Cell Reports

Article

ARHGAP12 and ARHGAP29 exert distinct regulatory effects on switching between two cell morphological states through GSK-3 activity

Graphical abstract

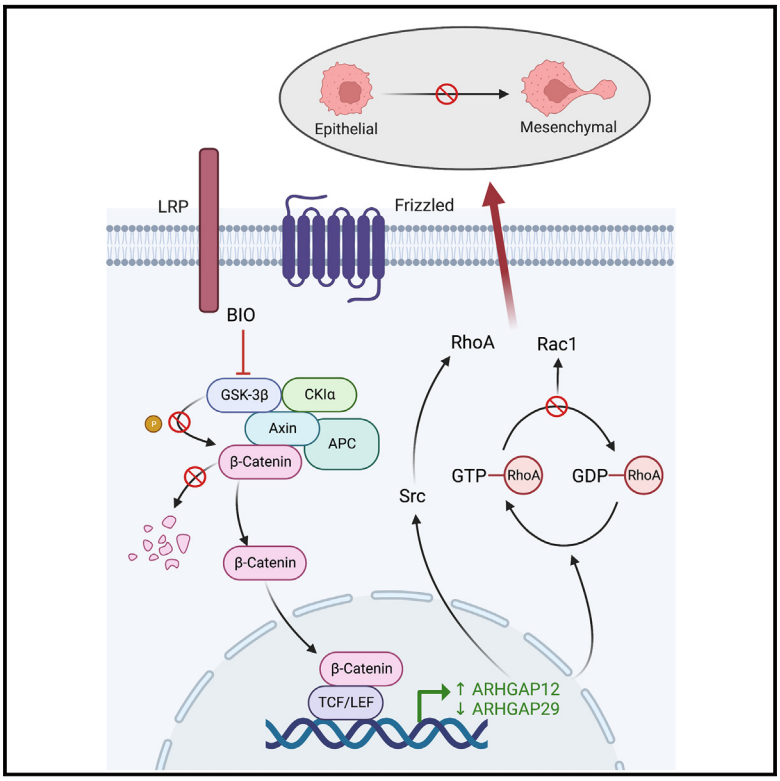

Highlights

- Inhibition of GSK-3 with BIO deregulates *ARHGAP* transcription in glioma cells
- *ARHGAP12* and *ARHGAP29* deregulation affects cell plasticity by targeting of Src kinases
- Cell plasticity, characterized by morphological changes, alters cell migration and invasion
- The ARHGAPs are of biological and clinical relevance in tumor recurrence

Authors

Vinton W.T. Cheng, Philippa Vaughn-Beaucaire, Gary C. Shaw, ..., Susan C. Short, Sean E. Lawler, Anke Brüning-Richardson

Correspondence

a.bruning-richardson@hud.ac.uk

In brief

Cheng et al. describe a signaling pathway that promotes cellular plasticity (a switch between a mesenchymal-like or ameboid cell morphology) in glioma cells via glycogen synthase kinase 3 (GSK-3) activity with a downstream effect on Src kinase signaling via RhoGTPase activating protein activity, including ARHGAP12 and ARHGAP29.

Cheng et al., 2025, Cell Reports *44*, 115361
March 25, 2025
https://doi.org/10.1016/j.celrep.2025.115361

CellPress

Cell Reports

CellPress
OPEN ACCESS

Article

ARHGAP12 and ARHGAP29 exert distinct regulatory effects on switching between two cell morphological states through GSK-3 activity

Vinton W.T. Cheng,[1,2] Philippa Vaughn-Beaucaire,[3] Gary C. Shaw,[1] Malte Kriegs,[4] Alastair Droop,[5] George Psakis,[3] Michel Mittelbronn,[6,7,8,9,10] Matt Humphries,[11] Filomena Esteves,[1] Josie Hayes,[12] Julia V. Cockle,[13] Sabine Knipp,[3,14] Arndt Rohwedder,[14,15] Azzam Ismail,[16] Ola Rominiyi,[17] Spencer J. Collis,[18] Georgia Mavria,[1] James Samarasekara,[19] John E. Ladbury,[15] Sophie Ketchen,[1,15] Ruth Morton,[1] Sarah Fagan,[3] Daniel Tams,[1] Katie Myers,[20] Connor McGarrity-Cottrell,[20] Mark Dunning,[20] Marjorie Boissinot,[1] George Michalopoulos,[3] Sally Prior,[3] Yun Wah Lam,[3] Ewan E. Morrison,[1] Susan C. Short,[1] Sean E. Lawler,[21] and Anke Brüning-Richardson[3,22,*]

[1]Leeds Institute of Medical Research, Wellcome Trust Brenner Building, University of Leeds, Leeds LS9 7TF, UK
[2]Institute of Cancer and Genomic Sciences, University of Birmingham, Birmingham B15 2TT, UK
[3]School of Applied Sciences, Joseph Priestley Building, University of Huddersfield, Huddersfield HD1 3DH, UK
[4]Department of Radiobiology & Radiation Oncology and UCCH Kinomics Core Facility, Hubertus Wald Tumorzentrum – University Cancer Center Hamburg (UCCH), University Medical Center Hamburg-Eppendorf, Martinistrasse 52, 20246 Hamburg, Germany
[5]Wellcome Trust Genome Campus, Wellcome Trust Institute, Hinxton CB10 1RQ, UK
[6]Luxembourg Centre of Neuropathology, Luxembourg Institute of Health, L-3555 Dudelange, Luxembourg
[7]National Center of Pathology (NCP), Laboratoire National de Santé (LNS), L-3555 Dudelange, Luxembourg
[8]Department of Life Sciences and Medicine (DLSM), University of Luxembourg, L-4362, 28 Esch-sur-Alzette, Luxembourg
[9]Luxembourg Centre for Systems Biomedicine (LCSB), University of Luxembourg, L-4362 Esch-sur-Alzette, Luxembourg
[10]Department of Cancer Research (DoCR), Luxembourg Institute of Health (LIH), L-1210 Luxembourg, Luxembourg
[11]National Pathology Imaging Cooperative, Leeds Teaching Hospitals NHS Trust, St James's University Hospital, Leeds LS9 7TF, UK
[12]REVOLUTION Medicines, Redwood City, California 94036, USA
[13]Institute of Cancer Research, London SW7 3RP, UK
[14]Zentrum fuer Medizinische Forschung, Johannes Kepler University, Linz, Austria
[15]School of Molecular and Cellular Biology, University of Leeds, Leeds LS2 9JT, UK
[16]Pathology Department, Leeds Teaching Hospitals NHS Trust, St James's University Hospital, Leeds LS9 7TF, UK
[17]Department of Neuroscience, School of Medicine and Population Health, University of Sheffield, Sheffield S10 2RX, UK
[18]Department of Clinical Medicine, School of Medicine and Population Health, University of Sheffield, Sheffield S10 2RX, UK
[19]Department of Neurosurgery, Queen's Hospital, London RM7 0AG, UK
[20]Sheffield Bioinformatics Core, Faculty of Health, University of Sheffield, Sheffield, S10 2RX, UK
[21]Department of Pathology & Laboratory Medicine, Legorreta Cancer Center, Brown University, Providence, Rhode Island 02903, USA
[22]Lead contact
*Correspondence: a.bruning-richardson@hud.ac.uk
https://doi.org/10.1016/j.celrep.2025.115361

SUMMARY

Cancer cells undergo morphological changes and phenotype switching to promote invasion into healthy tissues. Manipulating the transitional morphological states in cancer cells to prevent tumor dissemination may enhance survival and improve treatment response. We describe two members of the RhoGTPase activating protein (ARHGAP) family, ARHGAP12 and ARHGAP29, as regulators of transitional morphological states in glioma via Src kinase signaling events, leading to morphological changes that correspond to phenotype switching. Moreover, we establish a link between glycogen synthase kinase 3 (GSK-3) inhibition and β-catenin translocation in altering transcription of *ARHGAP12* and *ARHGAP29*. Silencing *ARHGAP12* causes loss of N-cadherin and adoption of mesenchymal morphology, a characteristic feature of aggressive cellular behavior. In patients with glioblastoma (GBM), we identify a link between ARHGAP12 and ARHGAP29 co-expression and recurrence after treatment. Consequently, we propose that further investigation of how ARHGAPs regulate transitional morphological events to drive cancer dissemination is warranted.

INTRODUCTION

The ability of cancer cells to alter cell morphology or display phenotypic switching is a crucial cellular mechanism that is aberrantly hijacked in cancer cells to mobilize and invade away from the tumor mass. In malignant brain tumors, a similar process, called glial-mesenchymal transition, is believed to occur, with distinct morphological transitional states in cancer cells driven

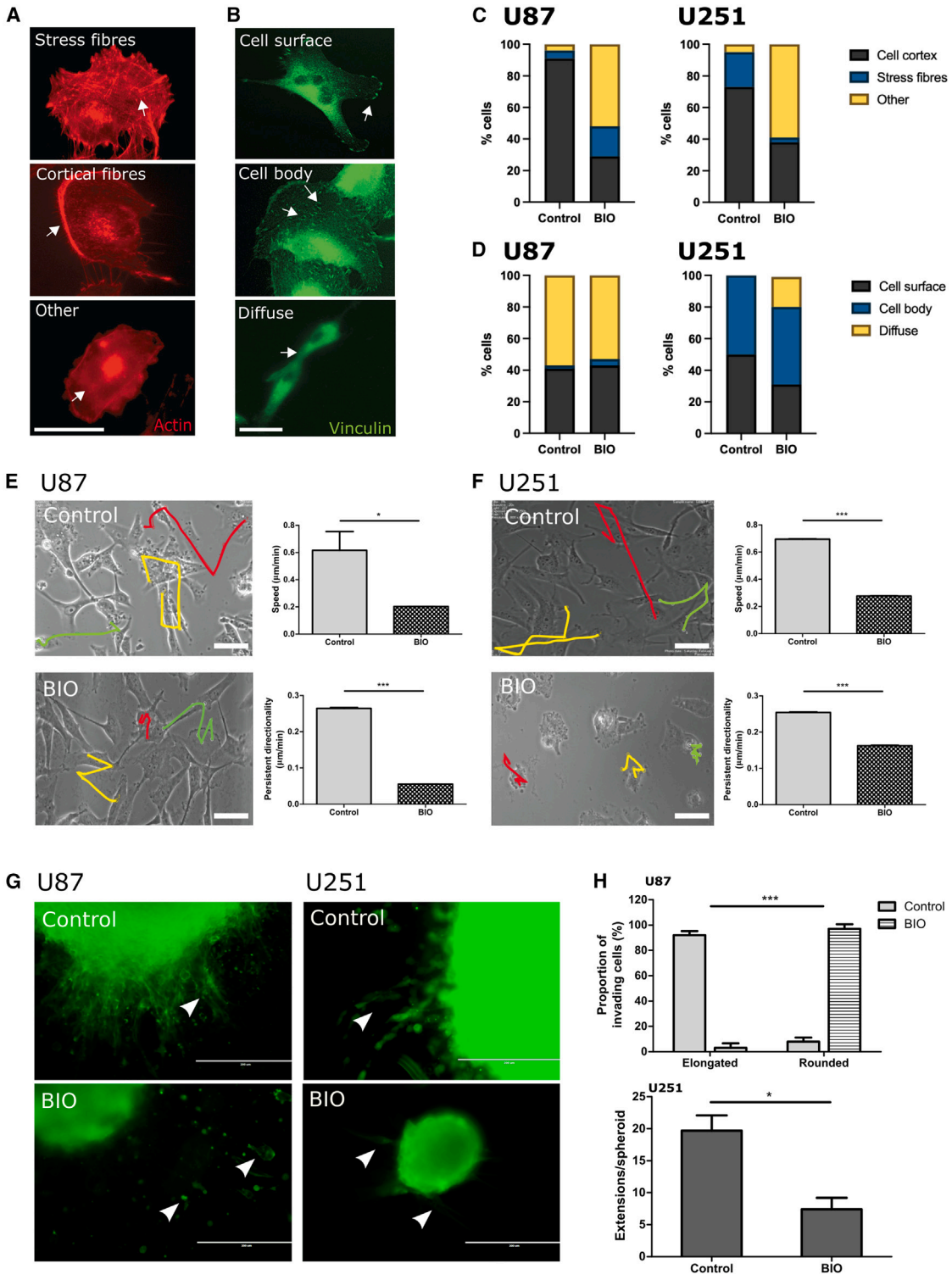

Figure 1. Inhibition with the GSK-3 inhibitor BIO targets actin cytoskeleton arrangements, inducing functional and morphological changes

(A) Actin localization in U251 glioma cells treated with a GSK-3 inhibitor showed three distinct patterns: stress fibers, cortical fibers, and unspecified perinuclear labeling ("other"). Scale bar: 10 μm.

(B) Conversely, a marker of focal adhesions was localized to either the cell surface or the whole cell body or was diffusely distributed with no discernible labeling. Scale bar: 10 μm.

(legend continued on next page)

by morphological plasticity.[1] This tendency to infiltrate into the surrounding brain parenchyma is a major contributor to the dismal prognosis associated with the most aggressive malignant brain tumor, glioblastoma (GBM), with greater than 90% of patients experiencing relapse within 5 years despite maximal multimodal therapy.[2]

Regulators of associated morphological plasticity and their mode of action are therefore of increasing interest to target cancer dissemination. Recently, utilizing small-molecule inhibitors of migratory signaling pathways to target cell migration/invasion in human GBM, we have reported that GBM cells undergo distinct morphological changes following exposure to these inhibitors.[3,4] Since cell morphology is a distinct characteristic of an epithelial/mesenchymal switch in invasive cancer cells, these initial observations encouraged us to explore a potential link with cellular plasticity and transitional morphological states in migratory cells. In particular, we had ascertained that 6-bromo-indirubin-3′-oxime (BIO), a synthetic derivative of the chemical compound indirubin, inhibits cell migration concomitant with distinct morphological changes associated with invasion in the affected cells.[3,5] BIO has been shown to exert its activity through inhibition of glycogen synthase kinase 3 (GSK-3), though the precise mode of action downstream of GSK-3 signaling has not been established.[6,7] Of note, Vijay et al. reported a relationship between GSK-3 activity and epithelial-mesenchymal transition (EMT) in epithelial-derived, triple-negative breast cancer. Furthermore, they showed that inhibition of GSK-3 using BIO led to the inhibition of EMT, although the precise mechanisms were not elucidated.[8]

It is known that downstream targets of GSK-3 include the RhoGTPases RhoA and Rac1, which are crucial for cell migration through their effects on cell contractility and the actin cytoskeleton.[9–11] These RhoGTPases are, in turn, negatively regulated by the activity of the RhoGTPase activating proteins (ARHGAPs), which catalyze the hydrolysis of guanosine triphosphate (GTP) to guanosine diphosphate (GDP), thereby converting the active GTP-bound form of GTPases to the inactive GDP-bound form.[12] Thus, ARHGAPs function as molecular switches that permit swift changes in the cytoskeletal structure in response to external stimuli. It follows that the ARHGAPs regulate Rac1 or RhoA to promote specific cytoskeletal arrangements to also allow the cells to undergo morphological switches from one phenotype to another and adopt a particular mode of migration. Recent gene expression analyses conducted by our group on cancer cell lines treated with GSK-3 inhibitors suggest dysregulation of specific members of the ARHGAP family.[13] To date, a direct interaction between the ARHGAPs and morphological switching to promote cell migration and invasion through GSK-3 signaling has not been described.

In this study, we show that ARHGAP expression is altered by GSK-3 signaling, leading to distinct cellular morphological characteristics and, in turn, disrupting cell migration. Moreover, we show that GSK-3 regulates ARHGAP expression through β-catenin signaling and via an as yet unreported effect on Src kinase downstream signaling rather than acting directly on the RhoGTPases. Finally, we show that ARGAP12 and 29 co-expression is associated with reduced survival in patients with GBM. Consequently, our data provide support for the concept that BIO, through direct action of GSK-3 inhibition on ARHGAP activity, exerts morphological changes and links ARHGAP activity to clinical outcomes in GBM.

RESULTS

GSK-3 inhibition profoundly alters cell morphology and inhibits GBM cell migration *in vitro*

We have shown previously that the chemical inhibition of GSK3 by BIO led to a decrease in glioma invasion by blocking migratory phenotypes.[5] Here, we investigated the effect of BIO on cytoskeletal rearrangement and morphological changes in the GBM cell lines U251 and U87, both well-established *in vitro* models for tumor growth and angiogenesis[14] and invasive growth patterns.[5,15] Immunocytochemistry of U251 and U87 cells, with or without BIO, revealed distinct distribution patterns of actin filaments (Figure 1A) and focal adhesions (Figure 1B). Two main actin filament localizations were observed, either associated with the cell cortex or present as stress fibers. We also classified cells as "other," where only diffuse peri-nuclear phalloidin labeling and no discernible actin filament localization was seen (Figure 1A). Focal adhesions were classified according to cell surface, cell body, or diffuse localization (Figure 1B). Treatment with BIO resulted in a significant change in the overall actin distribution in both U251 and U87 cells, characterized by the re-localization or loss of cortical actin or stress fibers (Figure 1C) (Fisher's exact test, $p < 0.0001$, U87 and U251). There was a significant shift in the distribution of focal adhesions from the baseline phenotypes, from cortical or whole body associated to a diffuse labeling with no discernible localization in the U251 cells (Fisher's exact test, $p < 0.0001$) (Figure 1D), mirroring the results seen after GSK-3 inhibition with BIO. However, U87 cells showed no significant redistribution of focal adhesions after BIO treatment ($p = 0.6506$) (Figure 1D).

In addition, both cell lines displayed two distinct patterns of cell migration. In a 2D environment, U251 cells exhibited

(C and D) Actin (C) and focal adhesion (D) phenotypes were scored for untreated control cells ($n = 3$ technical repeats/150 cells per repeat) after treatment with BIO. Addition of the GSK-3 inhibitor BIO reduces cell speed and persistent directionality for both (E) U87 and (F) U251 glioma cells. Colored lines (red, yellow, and green) denote the migratory paths of 3 different cells within 2D culture. Images depict outlines of migratory paths of individual cells during live-cell imaging. Student's t test, $^{*}p < 0.05$, $^{***}p < 0.0001$. Scale bar: 50 μm.

(G) After treatment with BIO, migrating U87 cells demonstrated loss of protrusions and elongated cells concomitant with an increase in the appearance of rounded single cells (white arrowheads) compared to untreated cells (white arrowheads) in a 3D environment. In contrast, migrating U251 cells maintained long cellular protrusions; however, these were decreased in number and length post treatment with BIO (white arrowheads). Scale bar: 200 μm.

(H) The observed phenotypes were scored for both U87 and U251 cell-generated spheroids (n = at least 30/group with three individual repeats). U87 cell analysis: Fisher's exact test, $^{***}p < 0.0001$; U251 cell analysis: Student's t test, $^{*}p < 0.05$.

Data represent 3 independent experiments and are presented as mean ± SEM.

classical mesenchymal migration, characterized by extensive lamellipodium formation with a pronounced cell rear and front (Figure S1Aii). Meanwhile, U87 cells demonstrated a looser attachment to the supporting matrix while adopting a distinctly pointed "push and pull" phenotype with a poorly defined migration front (Figure S1Ai). When cultured as tumor spheroids in a collagen-based 3D matrix, both cell lines formed chain-like protrusions/extensions of migrating cells away from the central mass. At the extremities of the cell extensions, isolated cells would break away and adopt an elongated morphology (Figures S1B and S1C), which was particularly pronounced in U251 cells (Figures S1B and S1C). To examine the impact of GSK-3 inhibition on glioma cell invasion capacity, we first measured their migration velocity and persistent directionality[16] on a 2D surface. In the U251 and U87 cells, mean cell velocities were measured as 0.6 μm/min and 0.7 μm/min, and directed migration was measured as 0.27 μm/min and 0.25 μm/min, respectively (Figures 1E and 1F). For both cell lines, these values were consistent with mesenchymal migratory activity, as reported previously,[17] in terms of velocity ($\leq$1 μm/min) and the presence of filopodium-like protrusions (Table S1). Treatment with BIO was associated with a significant reduction in velocity (U251 = 0.2 μm/min, U87 = 0.3 μm/min) and persistent directionality (U251 = 0.05 μm/min, U87 = 0.16 μm/min) in both cell lines within 24 h compared to the untreated state (Student's t test; U87, $p = 0.0413$; and U251, $p < 0.0001$) (Figures 1E and 1F). Moreover, BIO-treated U87 cells adopted a rounded morphology, displaying loss of lamellipodia and front-rear polarity (Figure S1Aiii), whereas U251 cells were characterized by a mixed phenotype of thin/elongated or rounded cells (Figure S1Aiv; Table S1). Live-cell imaging with cell tracker dyes (actin and α-tubulin) confirmed a change in cytoskeletal arrangement in U251 cells (Figure S1). The observed changes in cell morphology and migration were abolished following drug withdrawal.[18]

As reported previously, U87 and U251 cells migrated efficiently into type 1 collagen, which was significantly reduced following GSK-3 inhibition.[19] We routinely use this model, as it has been shown to mimic the GBM microenvironment; for example, a most recent work by Wang et al. showed that collagen alpha-2(I) chain, a chain of type I collagen, is secreted by glioma cells to allow invasion of these cells into the normal brain parenchyma, and they suggest this collagen as a target to suppress invasion.[20] In our 3D assay, BIO treatment in U87 cells reduced the length and number of chain-like protrusions, with a greater number of detached, rounded migrating cells (Figure 1G, arrowheads). U251 cells also adopted shortened chain-like protrusions (Figure 1G) that contained a mixture of rounded and elongated morphologies (Figure S1; Table S1). These changes were confirmed by immunocytochemistry; in U87 cells, there was an apparent loss of extensions with an increase in single rounded cells (two-way ANOVA, $p < 0.0001$), whereas in U251 cells, we noted a decrease in the number of extensions (Student's t test, $p = 0.0149$; Figures 1G and 1H).

Taken together, BIO treatment in GBM cells led to profound changes in cell morphology and migration kinetics both in 2D monolayer culture and in cells disseminating from 3D spheroids. These changes were accompanied by significant intracellular redistribution of actin filaments.

ARHGAP12 and ARHGAP29 expression and cellular morphology change in response to disrupted GSK3 function

To investigate the molecular basis of these changes, we conducted a genome-wide transcriptomic study on BIO-treated U251 cells as compared to a vehicle-treated control.[18] We identified five *ARHGAP* genes among the differentially expressed genes in response to BIO (*ARHGPA4*↑, *ARHGAP12*↑, *ARHGAP22*↓, *ARHGAP25*↑, and *ARHGAP29*↓). As proof of principle of a role of ARHGAPs in BIO-mediated phenotype switching, we focused on two ARHGAP members, ARHGAP12 and ARHGAP29, which regulate Rac1 and RhoA, respectively.[21–23] In our screen, *ARHGAP12* was found to be upregulated (2.22-fold change) and *ARHGAP29* to be downregulated (3.13-fold change) by BIO treatment (Table S2). From these data, we hypothesized that ARHGAP12 would inhibit switching to a migratory state to promote cell migration, while ARHGAP29 would promote switching via targeting RhoGTPase activity. To confirm the clinical relevance of these two proteins, publicly available The Cancer Genome Atlas Program (TCGA) data revealed that ARHGAP12 and ARHGAP29 are both expressed in GBM and a wide diversity of GBM cell lines, including both cell lines used in this study (Figure S2).

To establish a link between GSK-3 signaling and the ARHGAPs, we first investigated ARHGAP12 and ARHGAP29 protein localization and expression levels in both 2D monolayer cells and 3D spheroids before and after GSK-3 inhibition in the GBM cell lines (Figure 2). By 2D immunofluorescence, ARHGAP12 was localized to the cytoplasm of U251 cells, as reported previously.[24] GSK-3 inhibition significantly increased the expression of ARHGAP12 (mean fold change = 7.6, post hoc Bonferroni test, $p < 0.05$) in U251 cells (Figures 2A and 2B), consistent with our transcriptomics data. Strong labeling of ARHGAP29 was detected in both the nuclear and cytoplasmic compartments of U251 cells, with loss of cytoplasmic staining after GSK-3 inhibition (Figure 2C). BIO treatment also induced ARHGAP12 expression and reduced ARHGAP29 expression (Figure S3) in a patient-derived cell line, GCGR-E17, indicating that the observed effects of BIO on the expression of these two ARHGAPs were not unique to U251 cells but likely a general phenomenon in GBM. In addition, we obtained transcriptomics data of matched core versus edge patient-derived GBM samples, which indicated pronounced association of ARHGAP29 with the edge of the tumor samples and ARHGAP12 with the core (Figure S4), suggesting specific roles of the ARHGAPs within tumor cell populations. In 3D matrix-embedded BIO-treated tumor spheroids, we also observed diffuse cytoplasmic ARHGAP12 staining in the spheroid core and migrating cells at the periphery, which became more pronounced compared to tumor spheroids exposed to vehicle only (Figure 2D, arrows). By contrast, ARHGAP29 was expressed strongly in core-associated and migratory cells, while BIO-treated spheroids had reduced ARHGAP29 protein expression in both cell populations (Figure 2D).

Transient silencing of *ARHGAP12* and *ARHGAP29* gene expression confirmed their opposing roles in modulating cell morphology, with ARHGAP29 promoting an elongated, mesenchymal phenotype and ARHGAP12 a rounded, ameboid phenotype (Figures S5A–S5C). These specific morphological changes

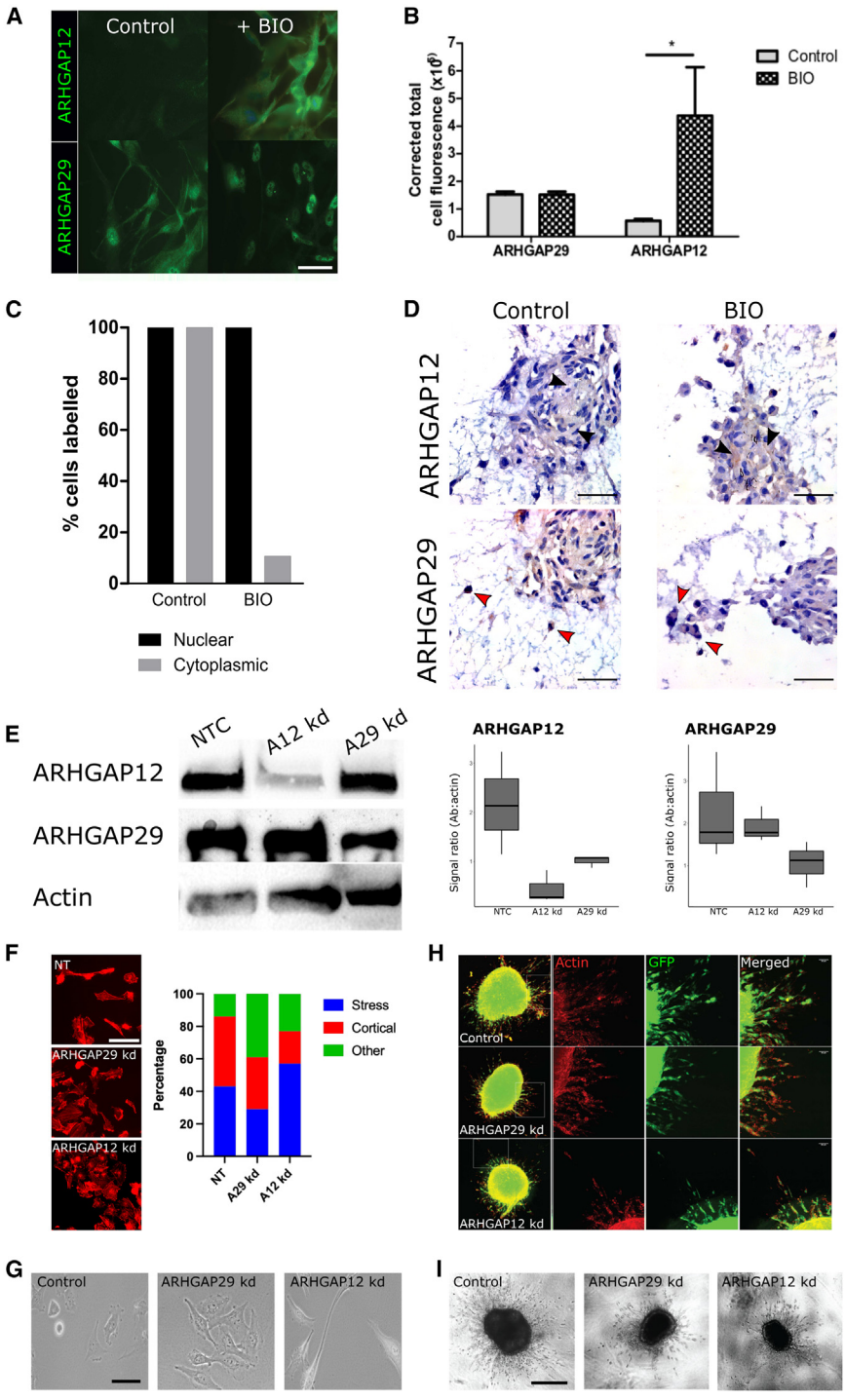

Figure 2. Gene expression analysis uncovers dysregulation of members of the *ARHGAP* gene family in U251 cells, and stable silencing of *ARHGAP12* and *ARHGAP29* in U251 cells exerts distinct cytoskeletal rearrangements

(A and B) Representative immunofluorescence images of ARHGAP12 and ARHGAP29 expression, untreated and after exposure to the GSK-3 inhibitor BIO (A), with quantification by total fluorescence (B). Student's t test, $*p < 0.05$. Scale bar: 10 μm. Data presented as mean ± SEM.

(C) Measurement of cellular localization showed loss of nuclear expression of both ARHGAP12 and ARHGAP29 following exposure to BIO.

(D) Representative bright-field micrographs of collagen-embedded U251 spheroids immunostained for either ARHGAP12 or ARHGAP29 (brown) and counterstained with hematoxylin. Cytoplasmic labeling of ARHGAP12 in the spheroid core became more pronounced after BIO treatment (black arrowheads). For ARHGAP29, cytoplasmic and membranous labeling was noted, especially on the spheroid periphery and on migratory cells, which was reduced after treatment with BIO (red arrowheads). Scale bar: 50 μm. Data presented as median.

(E) Stable gene silencing of *ARHGAP12* (A12 kd) and *ARHGAP29* (A29 kd) in U251 cells was confirmed by western blot.

(F) Representative immunofluorescence of U251 cells with stable *ARHGAP12* and *ARHGAP29* kd showing morphological changes and cytoskeletal rearrangement in U251 cells in 2D monolayers. Scale bar: 100 μm.

(G) Time-lapse microscopy of U251 cells with kd of the 2 different *ARHGAPs* showed distinct cellular morphological characteristics compared to control cells. Scale bar: 200 μm.

(H) In 3D spheroid assays, over 72 h, shorter cell protrusions consisting of rounded cells for the *ARHGAP29* kd and protrusions consisting of interconnected, elongated cells became evident. Scale bar: 100 μm.

(I) 3D invasion assays highlight cellular features and morphological changes of migrating cells after *ARHGHAP29* and *ARHGAP12* kd. Scale bar: 200 μm.

were also observed following the stable gene knockdown (kd) by shRNA (Figure 2E). In 2D monolayer culture of U251 cells, *ARHGAP12* kd cells were morphologically different from control cells; they were larger in size with pronounced stress fibers and loss of cortical actin (Figure 2F). The increase of actin fibers in *ARHGAP12* kd cells is consistent with the observed reduction of cortical actin and stress fibers after BIO treatment (Figure 1C), which upregulated *ARHGAP12* expression. In contrast, *ARHGAP29* kd cells appeared to be similar in size to the control and rounder than both wild-type and *ARHGAP12* kd cells (Figure 2F; Table S2), with more pronounced cortical, "pointy" actin localization. It is not clear why *ARHGAP29* kd did not mimic the actin distribution after BIO treatment. It is possible that the effect of *ARHGAP29* on actin distribution is highly sensitive to the precise expression level of this gene.

With live-cell imaging and by immunofluorescence, *ARHGAP29* kd cells were observed to maintain close proximity

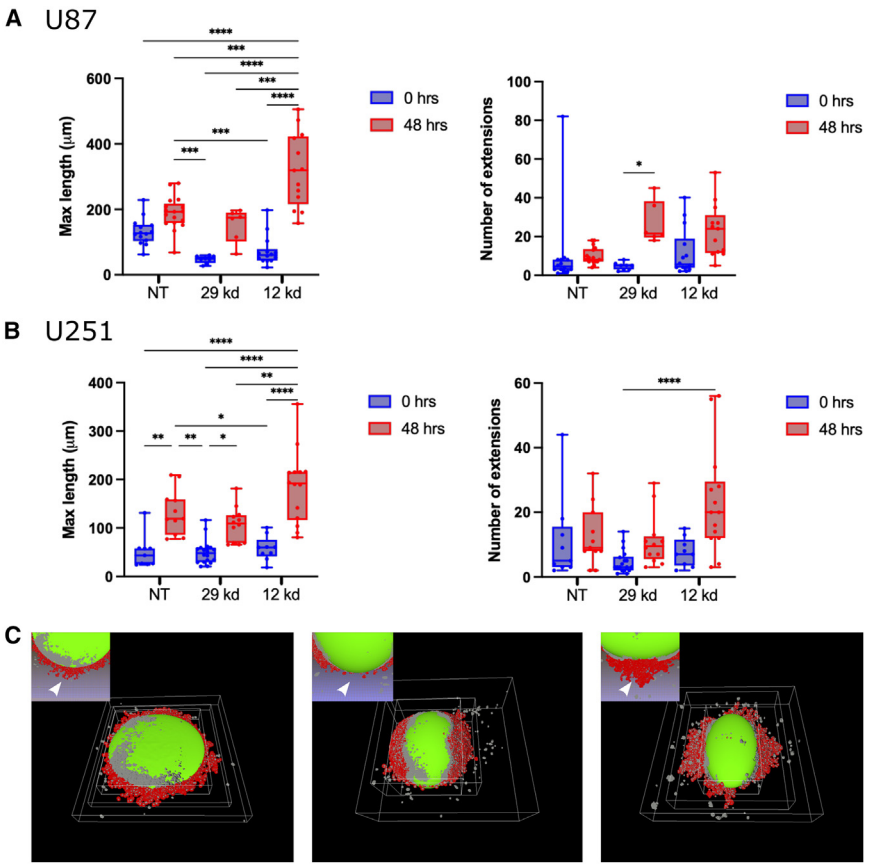

Figure 3. Stable silencing of *ARHGAP12* or *ARHGAP29* induces changes in the number of appendages emanating from spheroids and distance traveled away from spheroids by individual migratory cells

Using Cloudbuster software,[26] *ARHGAP12* and *ARHGAP29* kd cell spheroids were analyzed at time point 0 and at 48 h.

(A) In U87 cells, *ARHGAP29* kd spheroids showed reduced length of protrusions in comparison to *ARHGAP12* (one-way ANOVA, $p = 0.0002$) but no difference in the number of extensions after 48 h (one-way ANOVA, $p > 0.05$).

(B) For U251, a similar effect was seen after *ARHGAP12* kd in the length of cellular protrusions compared to *ARHGAP29* kd ($p = 0.0016$) after 48 h. Data presented as median, interquartile range.

(C) Representative reconstructed spheroids and migratory cells treated with a non-target control, *ARHGAP29* kd, or *ARHGAP12* kd. Insets highlight a selected region of an individual spheroid with visible extensions and individual cells (white arrowheads) with (left to right) a non-target (NT) control spheroid, *ARHGAP29* kd, and *ARHGAP12* kd.

with other cells, tending to form cellular "clumps," while wild-type and *ARHGAP12* kd cells appeared to be more dispersed (Figure 2H). In a 3D environment, migrating *ARHGAP29* kd cells disseminated from spheroids were also rounder than the counterparts in wild-type and *ARHGAP12* kd spheroids (Figures 2G and 2H; Table S3). These phenotypes are reminiscent of BIO-treated cells, suggesting that ARHGAP29 may play a role in mediating the BIO-induced changes in cell migration kinetics. By contrast, the *ARHGAP12* kd were elongated in 2D environments, or cells formed elongated chain-like extensions with single cells breaking away from the tumor cell mass in 3D environments (Figures 2H and 2I). Interestingly, cells disseminated from both *ARHGAP12* kd and *ARHGAP29* kd spheroids were significantly larger than wild-type cells (Table S3). In summary, loss of ARHGAP12 or ARHGAP29 expression led to distinct morphological characteristics in glioma cells and opposing migratory behavior, with inhibited invasion following *ARHGAP29* kd. Consistent with our findings in U251 cells, stable silencing of the two *ARHGAPs* in U87 GBM cells (Figure S6A) induced similar effects on cell shape and morphology (Figures S6B–S6E), with only discernible effect on cell migration in 3D after ARHGAP29 kd (Figures S6F and S6G).

Next, we assessed the effect of kd on cellular morphology in 3D spheroids in detail using the Cloudbuster software,[25] which allows the 3D reconstruction and quantification of stacked biological images (Figure 3). We confirmed that *ARHGAP29* kd negatively affected maximum and average length extension from U251 spheroids, whereas *ARHGAP12* kd appeared to promote the initial establishment of extensions, supporting the increased cellular connectivity observed in the spheroids (Figures 3A and 3B). U87 spheroid analysis demonstrated a reduction in the maximum length of extension for *ARHGAP29* kd and an increase in number and average length of cellular extensions for *ARHGAP12* kd (Figures 3A and 3B). Interestingly, 3D reconstruction of both U251 (Figure 3C) and U87 (data not shown) spheroids revealed a low cellular connectivity in the disseminating protrusions of both *ARHGAP12* and *ARHGAP29* kd, reminiscent of the increase of single disseminated cells in BIO-treated spheroids (Figures 1G and 1H).

In conclusion, both *ARHGAP12* and *ARHGAP29* kd had more profound impacts on cell morphology, associated with phenotype switching and cellular plasticity, than on cell velocity or cell invasion in 3D. This observation highlights the role of the two ARHGAPs in promoting a shift in migratory phenotype as part of eventual cell invasion, as evidenced by their effect on tumor extension dynamics. Based on these findings, we concluded that there are defined roles of ARHGAP12 and ARHGAP29 in processes enabling morphological switching, with an impact on cell invasion, regulated within a GSK-3 signaling network.

GSK-3 inhibition affects β-catenin-driven ARHGAP gene transcription

GSK-3 controls β-catenin-driven transcriptional programs by targeting β-catenin degradation. GSK-3 inhibition promotes the nuclear translocation of β-catenin, where it acts as transcription

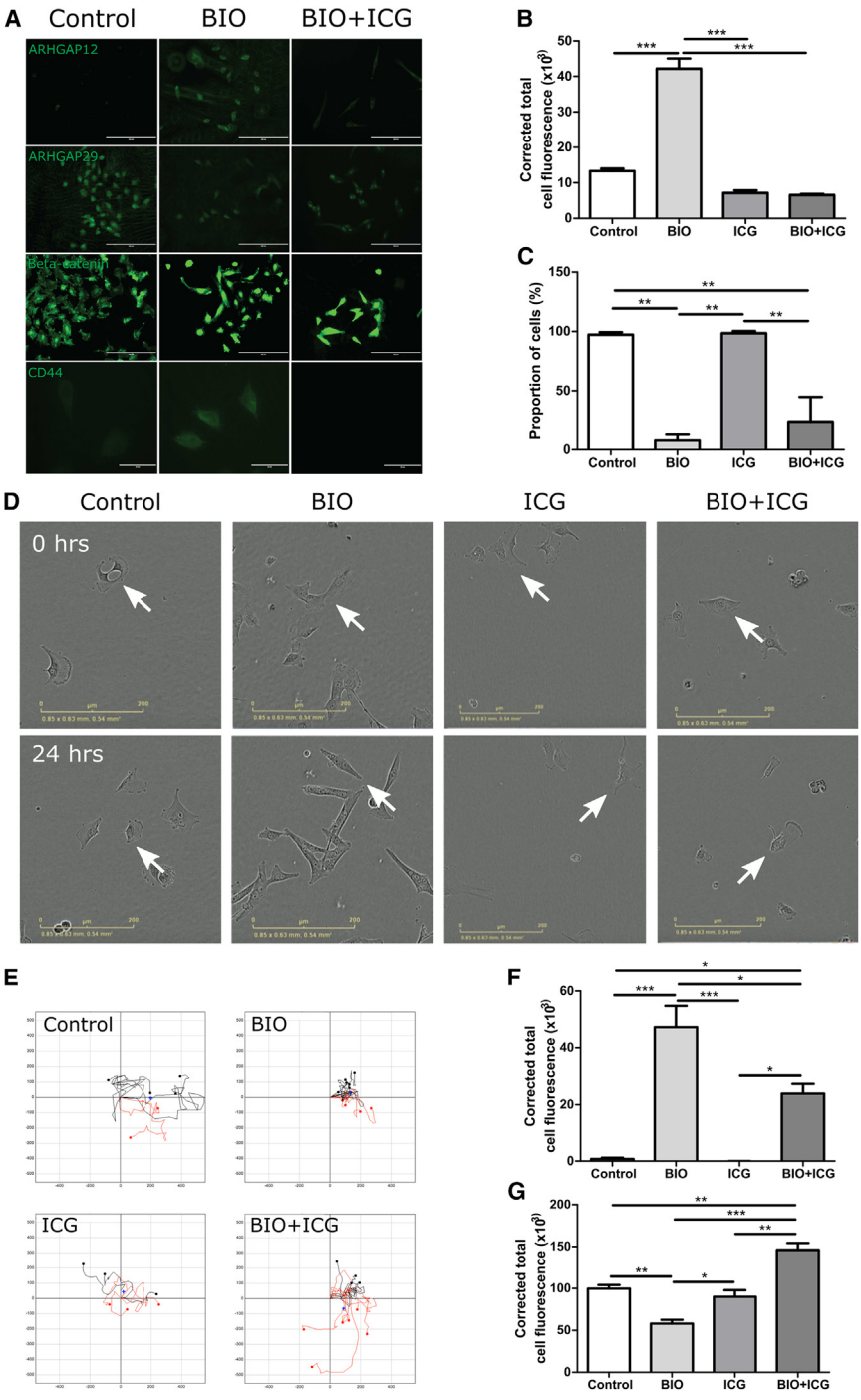

Figure 4. ARHGAP transcription is regulated in part by GSK-3 signaling via β-catenin translocation

(A) Immunofluorescence labeling with various markers (ARHGAP12, ARHGAP29, β-catenin, and CD44) of U251 cells treated with the GSK-3 inhibitor BIO. ICG001 and inhibitor combination reveals that ARHGAP12 and ARHGAP29 protein levels are altered after treatment with BIO and not affected by treatment with ICG001 alone or the combination treatment (n = 3/group). Scale bar: 200 μm.

(B and C) Significant differences (mean ± SEM) in (B) CD44 expression and (C) β-catenin expression in cell populations treated with the GSK-3 inhibitor BIO, ICG001, or ICG001 in combination with the GSK-3 inhibitor BIO were observed (n = 3). Data presented as mean ± SEM.

(D) Representative images from time-lapse microscopy of U251 cells, showing changes in the position of cells over a 24-h period in untreated, BIO-treated, ICG001-treated, and combination treatment groups. Scale bar: 200 μm

(E) Representative plots demonstrating the negative effect of the GSK inhibitor BIO on cell migration, with no effect of the inhibitor ICG001 and no effect after combination treatment.

(F and G) Significant differences (mean ± SEM) in (F) ARHGAP12 and (G) ARHGAP29 expression in cell populations treated with the GSK-3 inhibitor BIO, ICG001, or ICG001 in combination with the GSK-3 inhibitor BIO were observed (n = 3). Data presented as mean ± SEM.

Post hoc Dunnett's test, $^{*}p < 0.05$, $^{**}p < 0.01$, $^{***}p < 0.0001$.

factor regulating gene expression.[26] Therefore, we interrogated whether ARHGAP12 and ARHGAP29 expression was dependent on β-catenin functions by chemical inhibition of β-catenin-induced transcription (ICG001) in GBM cells. We confirmed that ICG001 reversed the BIO-induced expression of CD44, a β-catenin-regulated gene (Figures 4A and 4B), in U251 cells. ICG001 did not influence the increase of β-catenin expression (Figure 4A) and nuclear translocation (Figure 4C) in BIO-treated cells, suggesting that ICG001 suppressed β-catenin gene expression regulation without affecting the upstream mediation of β-catenin expression by GSK-3. Live-cell imaging of U251 cells revealed that, after 24 h of treatment, the altered morphological (Figure 4D) and migratory characteristics (Figure 4E) induced by BIO were abrogated with the addition of ICG001 (Table S4). While inhibition of the β-catenin pathway by ICG001 did not by itself affect ARHGAP12 and ARHGAP29 protein expression in U251, it significantly reduced the induction of ARHGAP12 expression by BIO (Figure 4F) and reversed the BIO-induced inhibition of ARHGAP29 expression (Figure 4G). Consequently, we conclude that *ARHGAP* gene transcription is regulated at least in part via the GSK-3/β-catenin signaling axis, with subsequent effects on cell morphology.

Effect of ARHGAP12 and ARHGAP29 kd on cellular signaling

To ascertain the role of the ARHGAPs in cellular signaling that resulted in morphological switching, we assessed the effect of

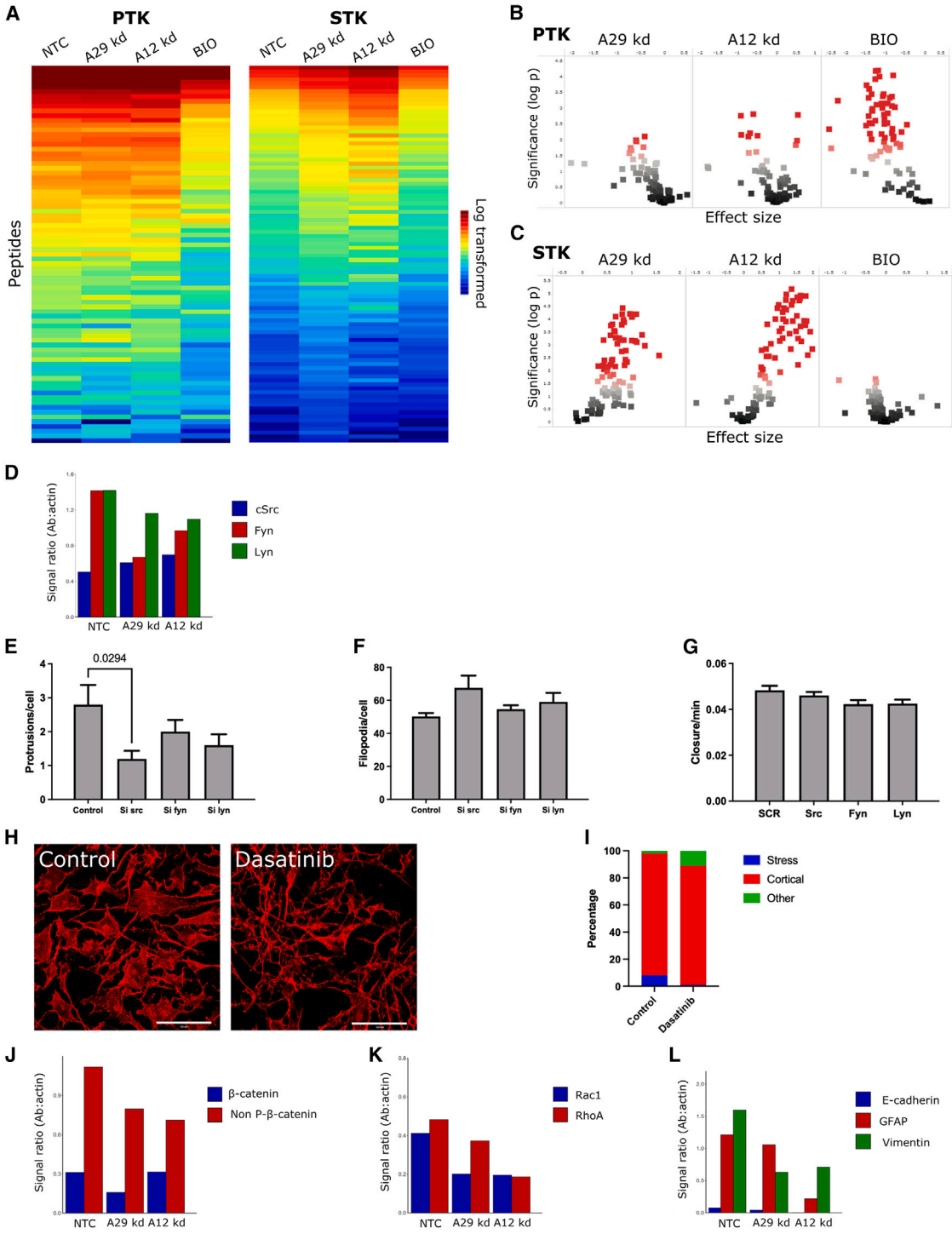

Figure 5. Kinome profiling demonstrates reduced PTK activity and increased STK activity in U251 *ARHGAP* kd cells

(A) Heatmaps showing log2-transformed signal intensities for the phosphorylated peptides ($n = 3$). The signals were sorted from high (red) to low (blue) intensity/phosphorylation.

(B and C) Two-group comparison of the wild type (NT) versus *AGHGAP* kd, depicted as a volcano plot (effect size < 0: lower phosphorylation in *ARHGAP* kd; significance score > 1.3 indicates significant changes). A BIO-treatment control is also included.

(D) Column graphs of SFKs depicting Src kinase levels (Src, Fyn and Lyn) by western blot.

(E and F) Quantification of U251 cell morphology with the ImageJ surface and direction detector plugin. The average number of (E) large protrusions and (F) filopodia detected in the control (scrambled) in comparison to siRNA-treated U251 cells targeting Fyn, Lyn, and Src is shown ($n = 3$ technical repeats), Post hoc

(legend continued on next page)

GSK3 inhibition on RhoA and Rac1 phosphorylation in U251 and U87 cells by a pull-down assay and G-LISA studies (Figure S7). We decided to focus first on RhoA activation in U251 cells, as we predicted an increase in RhoA phosphorylation after treatment with BIO. The pull-down assay indicated an increase in active RhoA; however, this result was not conclusive (Figure S7A). Therefore, we also performed G-LISA assays, which have proven high sensitivity and accuracy. Interestingly, while GSK inhibition by either BIO or AZD2858[27] did not induce significant changes in RhoA phosphorylation in either GBM cell line, these inhibitors dramatically increased Rac1 phosphorylation in U251 cells but reduced Rac1 phosphorylation in U87 cells (Figure S7B). These data indicate the effect of GSK3 activity on the functions of Ras GTPases. It is proposed that the observed effects on RhoA phosphorylation in different GBM cell lines are due to the combined effects of GSK3 inhibition on different ARHGAPs.

As ARHGAPs regulate the activity of the RhoGTPase family, which, in turn, regulates kinase-dependent signaling pathways,[28] we analyzed the effect of BIO treatment and *ARHGAP12* and *ARHGAP29* kd on the activities of protein tyrosine kinases (PTKs) and serine/threonine kinases (STKs) in U251 and U87 cells using specific phosphopeptide microarrays (Figures 5A, 5B, S8A, and S8B). Kd of both *ARHGAPs* reduced phosphorylation of several PTK-specific peptides, demonstrating impaired PTK activity (Figure S9), which was significant in U87 cells. Although the top 5 list of kinases demonstrated some heterogeneity, for each kd we observed reduced activity of at least 2 members of the Src family of kinases (SFK) (Figure S9). Thus, these data indicate that kd of *ARHGAP12* or *ARHGAP29* reduces SFK signaling. More heterogeneous effects were seen for STK activity following *ARHGAP* kd in U251 cells (Figures 5A and 5B). A dramatic activation of several STKs, alongside a significant increase in phosphorylation of many STK-specific peptides, was observed. The upstream kinase analysis showed good overlap, indicating comparable effects of *ARHGAP12* and *ARHGAP29* kd in U251 cells. Thus, despite some heterogeneity, functional kinome profiling demonstrated significant effects caused by *ARHGAP* kd involving several kinases, supporting their role in maintaining signal transduction.

Western blot analysis after gene silencing indicated that expression of the SFKs Src, Fyn, and Lyn changed in U251 cells after *ARHGAP12* and *ARHGAP29* silencing (Figure 5D). Src expression increased after each *ARHGAP* kd, whereas Fyn and Lyn expression decreased. Interestingly, small interfering RNA (siRNA) kd of Src in U251 cells led to a statistically significant loss of actin-driven protrusions ($p = 0.0294$, post hoc Dunnett's test), with a trend to increase in filopodia ($p = 0.0537$, post hoc Dunnett's test), but no significant reduction in the speed of wound closure (Figures 5E–5G), indicative of changes in EMT-like activity. We next analyzed the effect of the Src kinase inhibitor dasatinib on U87 and U251 cells. The effects of this inhibitor on actin distribution and localization have been reported previously.[29] Following treatment, we observed a pronounced relocalization of actin from stress fiber associated to cortical in both U87 and U251 cells, with both cell lines also exhibiting extensive filopodium formation on the cell surface (Figures 5H and 5I).

We also investigated β-catenin alongside vimentin (an EMT marker), RhoA, and Rac1 as potential downstream targets of ARHGAP activity and Src signaling. We observed a loss of non-phosphorylated β-catenin in response to kd of both *ARHGAPs* and a reduction in total β-catenin in the *ARHGAP29* kd, indicating that perturbations of ARHGAP12 and ARHGAP29 levels can affect β-catenin expression and levels. These data suggest, for the first time, an alternative mechanism by which GSK3 regulates β-catenin activity by targeting ARHGAP expression. *ARHGAP12* and *ARHGAP29* kd also reduced the levels of RhoA, Rac1 (Figures 5J and 5K), vimentin, and glial fibrillary acidic protein (GFAP), while E-cadherin (a transitional state marker) levels appeared to be the least affected (Figure 5L). The marked reduction in GFAP levels, a tumor marker, associated with *ARHGAP12* kd (Figure 5L) suggested the transition to a more aggressive state, whereas loss of vimentin may indicate a change to a more deformable morphology and invasive activity, as reported previously.[30,31]

Finally, functional kinome profiling after kd of *ARHGAP12* in U87 cells highlighted reduced phosphorylation of many peptides; *ARHGAP29* kd in U87 cells induced a significant reduction only for some peptides (Figures S8A and S8B). Moreover, analysis revealed similarities in the affected kinases, since reduced IKKE and Chk1 activity was predicted for kd of both *ARHGAPs* (data not shown). Src expression decreased after both kd in U87 cells, Fyn decreased after *ARHGAP12* kd and increased after *ARHGAP29* kd, and increased levels of Lyn were seen after *ARHGAP12* kd (Figure S8C). Changes in downstream targets of ARHGAP activity were also observed (Figures S8D–S8F).

ARHGAP12 and ARHGAP29 regulate cellular phenotype switching *in vivo*

To assess the role of ARHGAP activity on cellular events *in vivo*, we used an orthotopic intracranial xenograft mouse model. U87 cells are known to induce rapid tumor formation in mice.[32] We postulated that the previously observed *in vitro* phenotypes after *ARHGAP* kd would be more noticeable in this tumor type, where tumors are induced that characteristically possess low infiltration activity and are characterized by clear, well-demarcated tumor borders. We intracranially injected non-target control U87 cells and cells harboring either stable *ARHGAP12* or *ARHGAP29* kd and investigated the tumors that formed. All tumors stained strongly for vimentin, confirming tumor malignancy, although, in *ARHGAP29* kd tumors, the vimentin staining appeared to be less homogeneous compared to control and *ARHGAP12* kd (Figure 6A). Morphologically, *ARHGAP29* kd

Dunnett's test, $p < 0.05$. (G) Quantification of relative wound closure after siRNA exposure targeting Fyn, Lyn, and Src; Error bars indicate SEM ($n = 3$ technical repeats).

(H and I) Representative images of (H) actin relocalization after treatment with the Src kinase inhibitor dasatinib, with (I) loss of stress fibers and an increase in undefined "other" actin localization.

(J–L) β-catenin (J), Rho-family small GTPases (K), and EMT marker expression (L) after *ARHGAP12* and *ARHGAP29* kd. At least three independent western blot experiments were analyzed for each antibody.

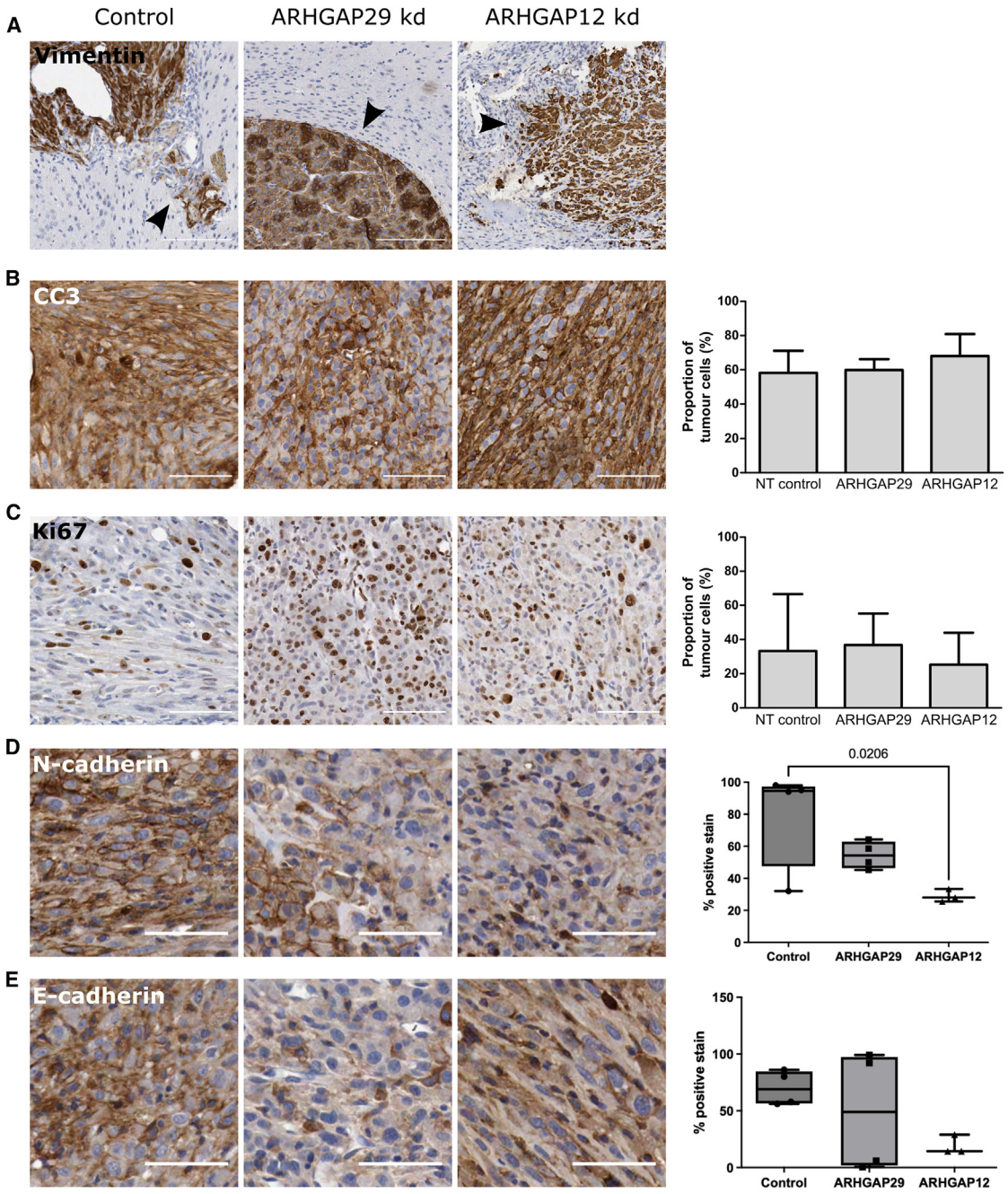

Figure 6. Intracranially injected *ARHGAP12* and *ARHGAP29* kd cells induce tumors with altered morphological features

(A–C) Representative mouse brain tissue sections of intracranial tumors from non-target control, *ARHGAP12* kd, and *ARHGAP29* kd cells with immunohistochemical staining (brown) and corresponding column graphs for expression of the following cell markers: (A) vimentin; (B) cleaved caspase-3 (CC3), an apoptosis marker; and (C) Ki67, expressed in proliferating cell nuclei. Black arrowheads indicate different morphological features of the tumor margin. Vimentin scale bar: 150 μm; CC3 and Ki67 scale bars: 75 μm. Data presented as mean ± SEM.

(D and E) Both (D) N-cadherin and (E) E-cadherin were strongly expressed on tumor cells in the control group, with a significant loss of N-cadherin expression in *ARHGAP12* kd tumors. Scale bar: 75 μm; post hoc Dunnett's test. Data presented as median, interquartile range, and range.

tumors were characterized by a smooth margin with few cellular protrusions or single cells in the adjacent brain parenchyma, in contrast to the margin of *ARHGAP12* kd tumors, where long extensions and single cells were observed (Figure 6A). Neither tumor cell proliferation (measured using Ki67 staining) nor cell death (assessed by cleaved caspase-3 [CC3] staining) were significantly affected by *ARHGAP* kd (Figures 6B and 6C). E-cadherin and N-cadherin, markers of transitional

morphological states, were differentially expressed in the kd tumors; both were highly expressed in control tumors, while N-cadherin expression was reduced in the *ARHGAP12* kd tumors (post hoc Dunnett's test, $p = 0.0206$) (Figures 6D and 6E).

Overall, there was cumulative evidence of a more aggressive, invasive phenotype in the tumors with silenced *ARHGAP12*, with evidence of increased morphological switching occurring in these tumors.

ARHGAP12 and ARHGAP29 co-expression is associated with disease recurrence after treatment

Given our *in vitro* and *in vivo* findings supporting the ARHGAPs as key regulators of migrating cancer cell morphology in a biological context, we next examined the clinical relevance of ARHGAP activity. We accessed publicly available data via Betastasis,[33] obtained from TCGA, and investigated protein expression and patient survival in all samples, stratified to four GBM subtypes: proneural, neural, classical, and mesenchymal. There was an association between high *ARHGAP29* expression and improved survival in the proneural group ($p = 0.0492$) (Figure S10A). Interestingly, for all GBM subtypes treated with chemotherapy, there was also a positive association between *ARHGAP29* expression and survival ($p = 0.0465$). An association between *ARHGAP12* expression and survival was noted in the proneural group ($p = 0.0291$) (Figure S10B). We further validated the clinical relevance of *ARHGAP* expression through a tissue microarray (TMA) of high-grade gliomas with associated clinical outcomes. In the TMAs, we observed cytoplasmic (ARHGAP12 and ARHGAP29) and cytoplasmic and membranous (ARHGAP29) staining in tissues from high-grade gliomas. We determined that ARHGAP12 and ARHGAP29 co-expression was negatively associated with disease recurrence after treatment ($p = 0.0105$) (Figures S10C and S10D). We also utilized the NIH NCI GBM Bio Discovery Portal (Glioma-BioDP; https://gbmbiodp.nci.nih.gov)[34,35] to confirm a role of co-expression and overall survival in GBM; we found a negative association between ARHGAP12 and ARHGAP29 co-expression and overall survival specifically in the proneural subgroup (Figure S11).

DISCUSSION

Cancer cell migration and invasion are highly complex processes involving the regulation of morphological changes. Regulators of morphological switches associated with cancer cell motility are of increasing interest to prevent recurrence of tumors to improve patient outcome. At the microstructural level, small RhoGTPases directly regulate actin dynamics, facilitating cytoskeletal reorganization toward either mesenchymal or ameboid migratory phenotypes with distinct morphological features, including the formation of elaborate lamellipodia or rounding with single filopodia and contractile rings.[36] Although associated morphological changes and cell migration have been well characterized in epithelial-derived tumors, the mechanisms of equivalent changes/switching and cell invasion in diffusely disseminating tumors like GBM are less clear.

We report a signaling pathway downstream of GSK-3 activity that regulates morphological changes in cancer cells to switch from one epithelial-like phenotype to a mesenchymal-like phenotype enabling cell migration. Our work uncovered an important role in this pathway of RhoGTPase regulators, the ARHGAPs, supporting the notion that different ARHGAPs have specific roles (with some apparent redundancies) in mediating cellular plasticity by regulating morphological switches from epithelial-like (ameboid) to mesenchymal. The *ARHGAPs* represent a large family of over 60 genes that encode the Rho GTPase activating proteins, which interact with RhoGTPases.[37] Aberrant signaling through RhoGTPases can drive carcinogenesis, and specific genetic mutations have been reported.[38–40] Evidence from recent publications also highlights the role of ARHGAP activity in cell proliferation and migration. A number of *ARHGAP* genes have been shown to be deleted or mutated in different disease states, including cancer, demonstrating their biological importance.[41,42] Here, we uncovered a role of ARHGAPs in cancer invasion via promotion of morphological changes in a highly infiltrative malignancy, GBM. Notably, a direct impact on disease recurrence was found.

The roles of two ARHGAPs with opposing regulatory activity in cell morphology were investigated. Recent publications indicate the relevance of these molecules in dissemination or invasive growth of solid tumors. ARHGAP29 has been implicated in the dissemination of solid tumors, such as breast cancer[43] and hepatocellular carcinoma, under control of the Hippo signaling pathway.[42] Furthermore, ARHGAP29 has been found to be significantly elevated in circulating tumor cells in pancreatic cancer mouse models.[44] Increased *ARHGAP29* expression is associated with shortened survival in patients with gastric cancer.[45] Most recently, ARHGAP29 was found to be associated with invasion in mesenchymal-transformed breast cancer cells.[43] A direct interaction between Yes-associated protein (YAP), under control of the Hippo pathway, and ARHGAP29 has been shown to cause F-actin destabilization via suppression of the RhoA-LIMK-cofilin (LIMK, LIM domain kinase 1) pathway.[42] Intriguingly, we uncovered ARHGAP29 regulation of members of the Src signaling pathway, which, in turn, are known to activate the YAP/TAZ (TAZ, transcriptional coactivator with PDZ-binding motif) axis.[46] Thus, our results suggest that there may also be specific relevance to Hippo/YAP/TAZ signaling in infiltrative cancers, which warrants further investigation.

ARHGAP12 has been identified as a transcriptional target of hepatocyte growth factor (HGF) via tyrosine kinase receptor signaling.[21] In turn, HGF activates Rac1, an important promoter of actin polymerization, whereas ARHGAP12 inactivates Rac1. Overexpression of ARHGAP12 has been shown to cause loss of cell scattering, invasion, and adhesion in response to HGF in breast, prostate, thyroid, and lung cancer cell lines, which was abrogated by *ARHGAP12* gene silencing, suggesting that activity downstream of HGF signaling is mediated by the transcriptional regulation of *ARHGAP12*.[21]

We have also uncovered a signaling pathway involved in ARHGAP activity. The role of STKs such as GSK-3 in cancer progression is well established.[47] Surprisingly, we did not find evidence of ARHGAP activity on RhoGTPases directly impacting morphological switching or cell migration. However, we revealed novel, as yet unreported ARHGAP activity on Src kinase signaling with downstream effects on cell morphology,

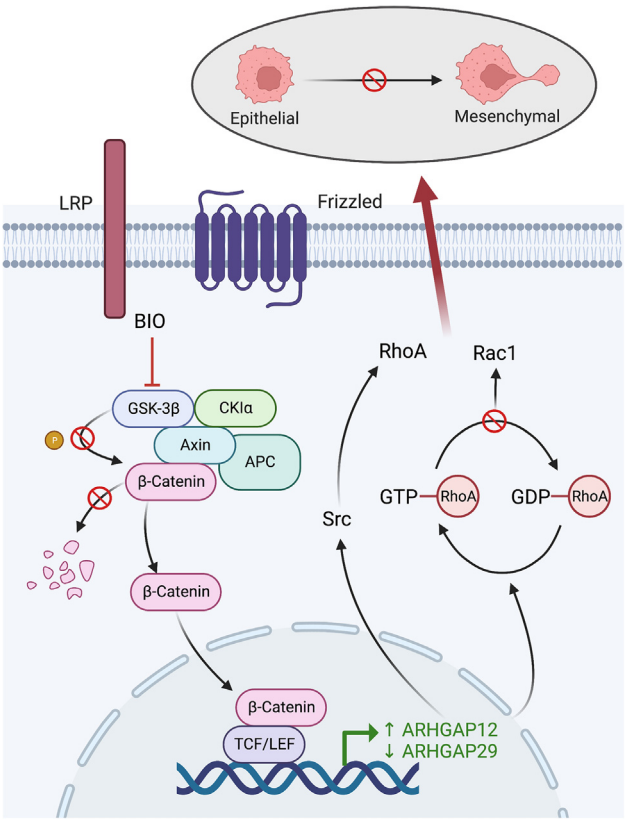

Figure 7. The ARHGAPs regulate glioma cell migration via a novel GSK-3 signaling pathway

Targeting GSK-3 activity with a small-molecule inhibitor (1) prevents β-catenin degradation by ubiquitination and (2) promotes β-catenin translocation to the nucleus, where it acts as a transcription factor. Transcription of *ARHGAP12* and prevention of transcription of *ARHGAP29* lead to changes in Src signaling and/or phosphorylation status of RhoA and Rac1 with (3) concomitant adoption of a less aggressive, ameboid phenotype in migratory cells. The phenotypic change in migrating cells may affect recurrence after surgery in patients.

potentially also involving RhoA and Rac1 via targeting of gene expression driving morphological changes. The role of the uncovered effects on PTKs after *ARHGAP* silencing needs to be further investigated, but this was beyond the scope of this study. Overall, based on the presented evidence, we propose a signaling pathway involving GSK-3 signaling via β-catenin translocation leading to *ARHGAP* gene transcription and regulation of kinase signaling such as Src (Figure 7). Interestingly, the overall effects of *ARHGAP* targeting cell morphology were found to be similar in both cell lines used in this study, despite their inherent phenotypic differences in migratory activity and associated morphological phenotype,[48,49] as was the effect of targeting GSK-3 activity. Intriguingly, the observed effects on cell extensions and protrusions in our 3D migration models are reminiscent of recent findings by Venkataramani et al., who described in great detail the presence of subpopulations of GBM cells forming a functional tumor cell network by microtubes. They also highlighted the presence of unconnected subpopulations of cells that promote whole-brain colonization.[50]

Our initial findings of ARHGAP activity and phenotypic effect on glioma cells *in vitro* were mirrored by our *in vivo* studies, and their importance was validated clinically in patient samples. Intriguingly, the role of morphological switching remains to be further elucidated in high-grade gliomas, as we noted loss of N-cadherin, a driver of EMT in solid tumor types, but with an apparent concomitant loss of tumor compactness within *ARHGAP12*-silenced tumors. The role of N-cadherin in transitional morphological changes in glioma is still debated; however, N-cadherin downregulation is believed to lead to altered cell polarization and abnormal motile behavior.[51] Other studies support the importance of members of the ARHGAP family in cellular processes such as EMT. For example, ARHGAP4 has been demonstrated to be a regulator of EMT-associated marker expression as well as cell migration and focal adhesion/stress fiber force generation.[52] ARHGAP4-controlled EMT processes have also been shown to be linked to activation of the FAK/Src (FAK, focal adhesion kinase) signaling pathway, mirroring some of the findings presented in our study.

In terms of clinical relevance, we found an association between *ARHGAP* expression and survival in the pro-neural subtype of GBM, where *ARHGAP12* expression was negatively associated with survival and *ARHGAP29* positively. This appears to contradict our suggestion of ARHGAP12 and ARHGAP29 as inhibiting or promoting transition to a more aggressive cellular state. The proneural GBM subtype is characterized by better survival in comparison to the other subtypes, with no significant difference in response to chemotherapy and radiotherapy. *IDH1* mutations are common in this type and promote abnormal cell growth. It may be speculated that, in these tumors, a prevention of transitioning to a more aggressive, infiltrative state enhances their proliferation capacity, thus negatively impacting survival. Co-expression of both ARHGAPs in our sample set consisting of high-grade tumors was associated with reduced time to recurrence, highlighting the inherent co-dependency of *ARHGAP* genes. Intriguingly, co-expression of both genes was also found to be associated with reduced overall survival in the pro-neural group, which may support the theory of proneural-mesenchymal transition, where recurrence of proneural tumors after treatment indicates a phenotypic shift to a more aggressive, mesenchymal subtype.[53] It may be argued that overexpression of both ARHGAP12 and ARHGAP29 will lead to the creation of a highly proliferative and migratory cell population, as observed for *HOXC6* overexpression in GBM by Yang et al., promoting concomitant tumor dissemination and growth.[54] Shimizu et al. also identified an association of ARHGAP29 with progression-free survival in prostate cancer and suggested ARHGAP29 as a prognostic biomarker and therapeutic target, underlining the relevance of the ARHGAPs in cancer progression.[55] Overall, our data support the hypothesis that cell phenotypes, in terms of morphology, reflect a balance between competing ARHGAP activities in a given cell type.

Given this, our findings raise challenging questions for the development of inhibitors specifically targeting regulators of phenotype switching and their associated signaling pathways; the development of such inhibitors must account for competing and co-dependent effects of ARHGAPs and the overall net effect of

combined ARHGAP function and potentially tumor-specific *ARHGAP* gene signatures on cell morphology and cellular transitional states.

Conclusion

We propose that a GSK-3-driven signaling network exists that leads to differential *ARHGAP* expression and induction of RhoGTPase-driven cytoskeletal arrangement activity involving Src signaling cascades to promote phenotype switching in tumors. Therefore, the ARHGAPs and their associated signaling pathways demand closer examination as regulators of cellular plasticity in cancer.

Limitations of the study

Our microarray data uncovered an ARHGAP signature consisting of five *ARHGAPs* that were dysregulated in a glioma cell line following BIO treatment. In this study, we focused on ARHGAP12 and ARHGAP29 and their role in glioma plasticity. Follow-up work on the other three ARHGAPs (ARHGAP4, ARHGAP22, and ARHGAP25) is ongoing. Furthermore, while our PamGene analysis uncovered a wealth of information regarding ARHGAP interactions with phosphotyrosine kinases and STKs, we focused solely on the STKs. Given the apparent concurrent effect of ARHGAP kd on phosphotyrosine kinases and the observed differential activity between two different cell lines, particularly in the cyclic AMP-dependent kinases, these initial findings will be explored further in subsequent lines of inquiry. Finally, although kd of *ARHGAP12* and *ARHGAP29* by both siRNA and shRNA yielded similar phenotypes, the levels of kd in these experiments were not very high. Cell lines with null ARHGAP mutations transfected with vectors that express inducible levels of ARHGAPs will allow a more quantitative investigation of the effect of these ARHGAPs on GBM cells in the future.

RESOURCE AVAILABILITY

Lead contact

Requests for further information and resources should be directed to and will be fulfilled by the lead contact, Anke Brüning-Richardson (a.bruning-richardson@hud.ac.uk).

Materials availability

All unique/stable reagents generated in this study are available from the lead contact with a completed materials transfer agreement.

Data and code availability

Raw microarray data have been deposited at BioStudies (EMBL-EBI) at https://www.ebi.ac.uk/biostudies/arrayexpress/studies/E-MTAB-12775, AccessionE-MTAB-12775, and are publicly available. Original western blot images, microscopic images/data, and PamGene data reported here will be shared by the lead contact upon request. This article does not report any original source code.

ACKNOWLEDGMENTS

We would like to dedicate this study to Pamela Roberts, the late Charity Director of the PPR Foundation, and to her late husband Peter, who passed away from a brain tumor. This study was financially supported by the PPR Foundation. The Cloudbuster-associated work was funded by the IBIN network. M.M. would like to thank the Luxembourg National Research Fund (FNR) for grant support (FNR PEARL P16/BM/11192868). The University of Huddersfield ICF Funds, United Kingdom, also financially contributed to this work. We would like to thank Dr Teklu Egnui for technical assistance.

AUTHOR CONTRIBUTIONS

Conceptualization, A.B.-R., S.C.S., and S.E.L.; methodology, A.B.-R., G.C.S., M.K., G.P., M.M., M.H., A.R., S. Knipp, S. Ketchen, F.E., J.H., O.R., S.J.C., K.M., C..M.-C, M.D., G. Mavria, G. Michalopoulos, S.P., S.C.S., and S.E.L.; software, A.B.-R. and A.R.; validation, P.V.-B., G.C.S., M.M., M.K., S. Knipp, A.R., J.S., S. Ketchen, and A.B.-R.; formal analysis, V.W.T.C., G.C.S., M.K., A.D., G.P., M.M., M.H., J.H., J.S., A.B.-R., Y.W.L.; investigation, P.V.-B., G.C.S., M.K., M.M., F.E., J.V.C., S. Knipp, A.R., A.I., J.S., M.B., D.T., S.F., R.M., S. Ketchen, and A.B.-R.; resources, A.B.-R., S.C.S., S.E.L., M.K., and M.M.; writing – original draft, V.W.T.C., A.B.-R., E.E.M., S.E.L., G.P., A.R., and A.D.; writing – review & editing, all authors; visualization, V.W.T.C., M.K., A.D., G.P., M.M., J.S., A.B.-R.; supervision, A.B.-R., S.C.S., S.E.L., M.K., and M.M.; project administration, A.B.-R., S.C.S., and S.E.L.; funding acquisition, A.B.-R., S.C.S., S.E.L., M.K., and M.M.

DECLARATION OF INTERESTS

The authors declare no competing interests.

STAR★METHODS

Detailed methods are provided in the online version of this paper and include the following:

- KEY RESOURCES TABLE
- EXPERIMENTAL MODEL AND STUDY PARTICIPANT DETAILS
  - Cell lines
  - *In vivo* experiments
  - GBM tissue microarray (TMA)
- METHOD DETAILS
  - Main reagents
  - Live cell imaging
  - Immunofluorescence assays
  - Bioinformatics
  - Microarray analysis
  - ARHGAP12 siRNA
  - ARHGAP29 siRNA
  - Real Time PCR
  - Small hairpin RNA
  - Phenotypic analysis for ARHGAP shRNA kd
  - Pulldown assay
  - Rac1/RhoA G-LISA
  - Functional kinome profiling
  - SDS-PAGE and western blotting
  - Src kinase siRNA studies
  - Quantification of relative wound closure speed
  - Src kinase inhibitor studies
  - Immunohistochemistry
  - Survival analysis of patient data
  - Immunohistochemistry spheroids
  - *In vivo* mouse brain tissue
  - Histological analysis
  - Surface roundness/smoothness of vimentin-stained tumors
  - Quantification of cell detachments from tumor mass
  - Analysis of single migratory cells and cell protrusions
  - TMA
- QUANTIFICATION AND STATISTICAL ANALYSIS
  - Statistical analysis

SUPPLEMENTAL INFORMATION

Supplemental information can be found online at https://doi.org/10.1016/j.celrep.2025.115361.

Received: February 16, 2024
Revised: December 26, 2024
Accepted: February 6, 2025
Published: March 6, 2025

REFERENCES

1. Azam, Z., To, S.S.T., and Tannous, B.A. (2020). Mesenchymal Transformation: The Rosetta Stone of Glioblastoma Pathogenesis and Therapy Resistance. Adv. Sci. *7*, 2002015. https://doi.org/10.1002/advs.202002015.
2. Stupp, R., Hegi, M.E., Mason, W.P., van den Bent, M.J., Taphoorn, M.J.B., Janzer, R.C., Ludwin, S.K., Allgeier, A., Fisher, B., Belanger, K., et al. (2009). Effects of radiotherapy with concomitant and adjuvant temozolomide versus radiotherapy alone on survival in glioblastoma in a randomised phase III study: 5-year analysis of the EORTC-NCIC trial. Lancet Oncol. *10*, 459–466. https://doi.org/10.1016/S1470-2045(09)70025-7.
3. Cockle, J.V., Picton, S., Levesley, J., Ilett, E., Carcaboso, A.M., Short, S., Steel, L.P., Melcher, A., Lawler, S.E., and Brüning-Richardson, A. (2015). Cell migration in paediatric glioma; characterisation and potential therapeutic targeting. Br. J. Cancer *112*, 693–703. https://doi.org/10.1038/bjc.2015.16.
4. Ketchen, S.E., Gamboa-Esteves, F.O., Lawler, S.E., Nowicki, M.O., Rohwedder, A., Knipp, S., Prior, S., Short, S.C., Ladbury, J.E., and Brüning-Richardson, A. (2021). Drug Resistance in Glioma Cells Induced by a Mesenchymal-Amoeboid Migratory Switch. Biomedicines *10*, 9. https://doi.org/10.3390/biomedicines10010009.
5. Williams, S.P., Nowicki, M.O., Liu, F., Press, R., Godlewski, J., Abdel-Rasoul, M., Kaur, B., Fernandez, S.A., Chiocca, E.A., and Lawler, S.E. (2011). Indirubins decrease glioma invasion by blocking migratory phenotypes in both the tumor and stromal endothelial cell compartments. Cancer Res. *71*, 5374–5380. https://doi.org/10.1158/0008-5472.CAN-10-3026.
6. Sklirou, A.D., Gaboriaud-Kolar, N., Papassideri, I., Skaltsounis, A.L., and Trougakos, I.P. (2017). 6-bromo-indirubin-3'-oxime (6BIO), a Glycogen synthase kinase-3beta inhibitor, activates cytoprotective cellular modules and suppresses cellular senescence-mediated biomolecular damage in human fibroblasts. Sci. Rep. *7*, 11713. https://doi.org/10.1038/s41598-017-11662-7.
7. Meijer, L., Skaltsounis, A.L., Magiatis, P., Polychronopoulos, P., Knockaert, M., Leost, M., Ryan, X.P., Vonica, C.A., Brivanlou, A., Dajani, R., et al. (2003). GSK-3-selective inhibitors derived from Tyrian purple indirubins. Chem. Biol. *10*, 1255–1266. https://doi.org/10.1016/j.chembiol.2003.11.010.
8. Vijay, G.V., Zhao, N., Den Hollander, P., Toneff, M.J., Joseph, R., Pietila, M., Taube, J.H., Sarkar, T.R., Ramirez-Pena, E., Werden, S.J., et al. (2019). GSK3beta regulates epithelial-mesenchymal transition and cancer stem cell properties in triple-negative breast cancer. Breast Cancer Res. *21*, 37. https://doi.org/10.1186/s13058-019-1125-0.
9. Haga, R.B., and Ridley, A.J. (2016). Rho GTPases: Regulation and roles in cancer cell biology. Small GTPases *7*, 207–221. https://doi.org/10.1080/21541248.2016.1232583.
10. Nguyen, L.K., Kholodenko, B.N., and von Kriegsheim, A. (2018). Rac1 and RhoA: Networks, loops and bistability. Small GTPases *9*, 316–321. https://doi.org/10.1080/21541248.2016.1224399.
11. Al-Koussa, H., Atat, O.E., Jaafar, L., Tashjian, H., and El-Sibai, M. (2020). The Role of Rho GTPases in Motility and Invasion of Glioblastoma Cells. Anal. Cell. Pathol. *2020*, 9274016. https://doi.org/10.1155/2020/9274016.
12. Amin, E., Jaiswal, M., Derewenda, U., Reis, K., Nouri, K., Koessmeier, K.T., Aspenström, P., Somlyo, A.V., Dvorsky, R., and Ahmadian, M.R. (2016). Deciphering the Molecular and Functional Basis of RHOGAP Family Proteins: A Systematic Approach Toward Selective Inactivation of Rho Family Proteins. J. Biol. Chem. *291*, 20353–20371. https://doi.org/10.1074/jbc.M116.736967.
13. Zdioruk, M., Jimenez-Macias, J.L., Nowicki, M.O., Manz, K.E., Pennell, K.D., Koch, M.S., Finkelberg, T., Wu, B., Boucher, P., Takeda, Y., et al. (2023). PPRX-1701, a nanoparticle formulation of 6'-bromoindirubin acetoxime, improves delivery and shows efficacy in preclinical GBM models. Cell Rep. Med. *4*, 101019. https://doi.org/10.1016/j.xcrm.2023.101019.
14. Schulz, J.A., Rodgers, L.T., Kryscio, R.J., Hartz, A.M.S., and Bauer, B. (2022). Characterization and comparison of human glioblastoma models. BMC Cancer *22*, 844. https://doi.org/10.1186/s12885-022-09910-9.
15. Nowicki, M.O., Dmitrieva, N., Stein, A.M., Cutter, J.L., Godlewski, J., Saeki, Y., Nita, M., Berens, M.E., Sander, L.M., Newton, H.B., et al. (2008). Lithium inhibits invasion of glioma cells; possible involvement of glycogen synthase kinase-3. Neuro Oncol. *10*, 690–699. https://doi.org/10.1215/15228517-2008-041.
16. Gorelik, R., and Gautreau, A. (2014). Quantitative and unbiased analysis of directional persistence in cell migration. Nat. Protoc. *9*, 1931–1943. https://doi.org/10.1038/nprot.2014.131.
17. Bear, J.E., and Haugh, J.M. (2014). Directed migration of mesenchymal cells: where signaling and the cytoskeleton meet. Curr. Opin. Cell Biol. *30*, 74–82. https://doi.org/10.1016/j.ceb.2014.06.005.
18. Droop, A., Lawler, S., and Brüning-Richardson, A. (2023). The Effects of Antimigratory Drugs Lithium Chloride and 6-Bromoindirubin-3'-Oxime (BIO) in Glioblastoma Cells (BioStudies).
19. Cheng, V., Esteves, F., Chakrabarty, A., Cockle, J., Short, S., and Brüning-Richardson, A. (2015). High-content analysis of tumour cell invasion in three-dimensional spheroid assays. Oncoscience *2*, 596–606. https://doi.org/10.18632/oncoscience.171.
20. Wang, Y., Sakaguchi, M., Sabit, H., Tamai, S., Ichinose, T., Tanaka, S., Kinoshita, M., Uchida, Y., Ohtsuki, S., and Nakada, M. (2023). COL1A2 inhibition suppresses glioblastoma cell proliferation and invasion. J. Neurosurg. *138*, 639–648. https://doi.org/10.3171/2022.6.JNS22319.
21. Gentile, A., D'Alessandro, L., Lazzari, L., Martinoglio, B., Bertotti, A., Mira, A., Lanzetti, L., Comoglio, P.M., and Medico, E. (2008). Met-driven invasive growth involves transcriptional regulation of Arhgap12. Oncogene *27*, 5590–5598. https://doi.org/10.1038/onc.2008.173.
22. Saras, J., Franzén, P., Aspenström, P., Hellman, U., Gonez, L.J., and Heldin, C.H. (1997). A novel GTPase-activating protein for Rho interacts with a PDZ domain of the protein-tyrosine phosphatase PTPL1. J. Biol. Chem. *272*, 24333–24338. https://doi.org/10.1074/jbc.272.39.24333.
23. Myagmar, B.E., Umikawa, M., Asato, T., Taira, K., Oshiro, M., Hino, A., Takei, K., Uezato, H., and Kariya, K.i. (2005). PARG1, a protein-tyrosine phosphatase-associated RhoGAP, as a putative Rap2 effector. Biochem. Biophys. Res. Commun. *329*, 1046–1052. https://doi.org/10.1016/j.bbrc.2005.02.069.
24. Diring, J., Mouilleron, S., McDonald, N.Q., and Treisman, R. (2019). RPEL-family rhoGAPs link Rac/Cdc42 GTP loading to G-actin availability. Nat. Cell Biol. *21*, 845–855. https://doi.org/10.1038/s41556-019-0337-y.
25. Rohwedder, A., Knipp, S., Esteves, F.O., Hale, M., Ketchen, S.E., Treanor, D., and Brüning-Richardson, A. (2022). 'Cloudbuster': a Python-based open source application for three-dimensional reconstruction and quantification of stacked biological imaging samples. Interface Focus *12*, 20220016. https://doi.org/10.1098/rsfs.2022.0016.
26. Jamieson, C., Sharma, M., and Henderson, B.R. (2014). Targeting the beta-catenin nuclear transport pathway in cancer. Semin. Cancer Biol. *27*, 20–29. https://doi.org/10.1016/j.semcancer.2014.04.012.
27. Marsell, R., Sisask, G., Nilsson, Y., Sundgren-Andersson, A.K., Andersson, U., Larsson, S., Nilsson, O., Ljunggren, O., and Jonsson, K.B. (2012). GSK-3 inhibition by an orally active small molecule increases bone mass in rats. Bone *50*, 619–627. https://doi.org/10.1016/j.bone.2011.11.007.
28. Prudnikova, T.Y., Rawat, S.J., and Chernoff, J. (2015). Molecular pathways: targeting the kinase effectors of RHO-family GTPases. Clin. Cancer Res. *21*, 24–29. https://doi.org/10.1158/1078-0432.CCR-14-0827.

29. Lewis-Tuffin, L.J., Feathers, R., Hari, P., Durand, N., Li, Z., Rodriguez, F.J., Bakken, K., Carlson, B., Schroeder, M., Sarkaria, J.N., and Anastasiadis, P.Z. (2015). Src family kinases differentially influence glioma growth and motility. Mol. Oncol. *9*, 1783–1798. https://doi.org/10.1016/j.molonc.2015.06.001.

30. Battaglia, R.A., Delic, S., Herrmann, H., and Snider, N.T. (2018). Vimentin on the move:†new developments in cell migration[version 1; peer review: 2 approved]. F1000Res. *7*, F1000 Faculty Rev-1796. https://doi.org/10.12688/f1000research.15967.1.

31. Strouhalova, K., Přechová, M., Gandalovičová, A., Brábek, J., Gregor, M., and Rosel, D. (2020). Vimentin Intermediate Filaments as Potential Target for Cancer Treatment. Cancers *12*, 184.

32. Carcaboso, A.M., Elmeliegy, M.A., Shen, J., Juel, S.J., Zhang, Z.M., Calabrese, C., Tracey, L., Waters, C.M., and Stewart, C.F. (2010). Tyrosine kinase inhibitor gefitinib enhances topotecan penetration of gliomas. Cancer Res. *70*, 4499–4508. https://doi.org/10.1158/0008-5472.CAN-09-4264.

33. Betastasis, P. http://www.betastasis.com.

34. Celiku, O., Johnson, S., Zhao, S., Camphausen, K., and Shankavaram, U. (2014). Visualizing molecular profiles of glioblastoma with GBM-BioDP. PLoS One *9*, e101239. https://doi.org/10.1371/journal.pone.0101239.

35. Deng, X., Das, S., Kaur, H., Wilson, E., Camphausen, K., and Shankavaram, U. (2023). Glioma-BioDP: database for visualization of molecular profiles to improve prognosis of brain cancer. BMC Med. Genomics *16*, 168. https://doi.org/10.1186/s12920-023-01593-w.

36. Talkenberger, K., Cavalcanti-Adam, E.A., Voss-Böhme, A., and Deutsch, A. (2017). Amoeboid-mesenchymal migration plasticity promotes invasion only in complex heterogeneous microenvironments. Sci. Rep. *7*, 9237. https://doi.org/10.1038/s41598-017-09300-3.

37. Tcherkezian, J., and Lamarche-Vane, N. (2007). Current knowledge of the large RhoGAP family of proteins. Biol. Cell *99*, 67–86. https://doi.org/10.1042/BC20060086.

38. Zohn, I.M., Campbell, S.L., Khosravi-Far, R., Rossman, K.L., and Der, C.J. (1998). Rho family proteins and Ras transformation: the RHOad less traveled gets congested. Oncogene *17*, 1415–1438. https://doi.org/10.1038/sj.onc.1202181.

39. Benitah, S.A., Valerón, P.F., van Aelst, L., Marshall, C.J., and Lacal, J.C. (2004). Rho GTPases in human cancer: an unresolved link to upstream and downstream transcriptional regulation. Biochim. Biophys. Acta *1705*, 121–132. https://doi.org/10.1016/j.bbcan.2004.10.002.

40. Durkin, M.E., Yuan, B.Z., Zhou, X., Zimonjic, D.B., Lowy, D.R., Thorgeirsson, S.S., and Popescu, N.C. (2007). DLC-1:a Rho GTPase-activating protein and tumour suppressor. J. Cell Mol. Med. *11*, 1185–1207. https://doi.org/10.1111/j.1582-4934.2007.00098.x.

41. Huang, G.H., Sun, Z.L., Li, H.J., and Feng, D.F. (2017). Rho GTPase-activating proteins: Regulators of Rho GTPase activity in neuronal development and CNS diseases. Mol. Cell. Neurosci. *80*, 18–31. https://doi.org/10.1016/j.mcn.2017.01.007.

42. Chen, W.X., Lou, M., Cheng, L., Qian, Q., Xu, L.Y., Sun, L., Zhu, Y.L., and Dai, H. (2019). Bioinformatics analysis of potential therapeutic targets among ARHGAP genes in breast cancer. Oncol. Lett. *18*, 6017–6025. https://doi.org/10.3892/ol.2019.10949.

43. Kolb, K., Hellinger, J., Kansy, M., Wegwitz, F., Bauerschmitz, G., Emons, G., and Gründker, C. (2020). Influence of ARHGAP29 on the Invasion of Mesenchymal-Transformed Breast Cancer Cells. Cells *9*, 2616. https://doi.org/10.3390/cells9122616.

44. Qiao, Y., Chen, J., Lim, Y.B., Finch-Edmondson, M.L., Seshachalam, V.P., Qin, L., Jiang, T., Low, B.C., Singh, H., Lim, C.T., and Sudol, M. (2017). YAP Regulates Actin Dynamics through ARHGAP29 and Promotes Metastasis. Cell Rep. *19*, 1495–1502. https://doi.org/10.1016/j.celrep.2017.04.075.

45. Sudol, M. (2019). The Role of YAP Oncogene in Metastasis and Mechanomedicine. FASEB J. *33*, 620.12. https://doi.org/10.1096/fasebj.2019.33.1_supplement.620.12.

46. Lamar, J.M., Xiao, Y., Norton, E., Jiang, Z.G., Gerhard, G.M., Kooner, S., Warren, J.S.A., and Hynes, R.O. (2019). SRC tyrosine kinase activates the YAP/TAZ axis and thereby drives tumor growth and metastasis. J. Biol. Chem. *294*, 2302–2317. https://doi.org/10.1074/jbc.RA118.004364.

47. Domoto, T., Pyko, I.V., Furuta, T., Miyashita, K., Uehara, M., Shimasaki, T., Nakada, M., and Minamoto, T. (2016). Glycogen synthase kinase-3beta is a pivotal mediator of cancer invasion and resistance to therapy. Cancer Sci. *107*, 1363–1372. https://doi.org/10.1111/cas.13028.

48. Li, H., Lei, B., Xiang, W., Wang, H., Feng, W., Liu, Y., and Qi, S. (2017). Differences in Protein Expression between the U251 and U87 Cell Lines. Turk. Neurosurg. *27*, 894–903. https://doi.org/10.5137/1019-5149.JTN.17746-16.1.

49. Vogel, T.W., Zhuang, Z., Li, J., Okamoto, H., Furuta, M., Lee, Y.S., Zeng, W., Oldfield, E.H., Vortmeyer, A.O., and Weil, R.J. (2005). Proteins and protein pattern differences between glioma cell lines and glioblastoma multiforme. Clin. Cancer Res. *11*, 3624–3632. https://doi.org/10.1158/1078-0432.CCR-04-2115.

50. Venkataramani, V., Yang, Y., Schubert, M.C., Reyhan, E., Tetzlaff, S.K., Wißmann, N., Botz, M., Soyka, S.J., Beretta, C.A., Pramatarov, R.L., et al. (2022). Glioblastoma hijacks neuronal mechanisms for brain invasion. Cell *185*, 2899–2917.e31. https://doi.org/10.1016/j.cell.2022.06.054.

51. Noronha, C., Ribeiro, A.S., Taipa, R., Castro, D.S., Reis, J., Faria, C., and Paredes, J. (2021). Cadherin Expression and EMT: A Focus on Gliomas. Biomedicines *9*, 1328. https://doi.org/10.3390/biomedicines9101328.

52. Kang, N., Matsui, T.S., Liu, S., Fujiwara, S., and Deguchi, S. (2020). Comprehensive analysis on the whole Rho-GAP family reveals that ARHGAP4 suppresses EMT in epithelial cells under negative regulation by Septin9. FASEB J. *34*, 8326–8340. https://doi.org/10.1096/fj.201902750RR.

53. Fedele, M., Cerchia, L., Pegoraro, S., Sgarra, R., and Manfioletti, G. (2019). Proneural-Mesenchymal Transition: Phenotypic Plasticity to Acquire Multitherapy Resistance in Glioblastoma. Int. J. Mol. Sci. *20*, 2746. https://doi.org/10.3390/ijms20112746.

54. Yang, P., Kang, W., Pan, Y., Zhao, X., and Duan, L. (2019). Overexpression of HOXC6 promotes cell proliferation and migration via MAPK signaling and predicts a poor prognosis in glioblastoma. Cancer Manag. Res. *11*, 8167–8179. https://doi.org/10.2147/CMAR.S209904.

55. Shimizu, K., Matsumoto, H., Hirata, H., Ueno, K., Samoto, M., Mori, J., Fujii, N., Kawai, Y., Inoue, R., Yamamoto, Y., et al. (2020). ARHGAP29 expression may be a novel prognostic factor of cell proliferation and invasion in prostate cancer. Oncol. Rep. *44*, 2735–2745. https://doi.org/10.3892/or.2020.7811.

56. Pollard, S.M., Yoshikawa, K., Clarke, I.D., Danovi, D., Stricker, S., Russell, R., Bayani, J., Head, R., Lee, M., Bernstein, M., et al. (2009). Glioma stem cell lines expanded in adherent culture have tumor-specific phenotypes and are suitable for chemical and genetic screens. Cell Stem Cell *4*, 568–580. https://doi.org/10.1016/j.stem.2009.03.014.

57. Rominiyi, O., McGarrity-Cottrell, C., Myers, K.N., Jones, C.G., Wosnitzka, K., Williams, S.T., Vanderlinden, A., Antohi, A.G., Gomez-Roman, N., Chalmers, A.J., et al. (2024). Ex-vivo†models of post-surgical residual disease in human glioblastoma[version 1; peer review: 2 approved with reservations]. F1000Res. *13*, 1316. https://doi.org/10.12688/f1000research.157013.1.

58. Yang, Y.H., and Thorne, N.P. (2003). Normalization for two-color cDNA microarray data. In Science and Statistics: A Festschrift for Terry Speed, IMS Lecture Notes – Monograph Series, D.R. Goldstein, ed. (Institute of Mathematical Statistics), pp. 403–418.

59. Mittelbronn, M., Platten, M., Zeiner, P., Dombrowski, Y., Frank, B., Zachskorn, C., Harter, P.N., Weller, M., and Wischhusen, J. (2011). Macrophage migration inhibitory factor (MIF) expression in human malignant

gliomas contributes to immune escape and tumour progression. Acta Neuropathol. *122*, 353–365. https://doi.org/10.1007/s00401-011-0858-3.

60. Rueden, C.T., Schindelin, J., Hiner, M.C., DeZonia, B.E., Walter, A.E., Arena, E.T., and Eliceiri, K.W. (2017). ImageJ2: ImageJ for the next generation of scientific image data. BMC Bioinf. *18*, 529. https://doi.org/10.1186/s12859-017-1934-z.
61. Meijering, E., Dzyubachyk, O., and Smal, I. (2012). Methods for cell and particle tracking. Methods Enzymol. *504*, 183–200. https://doi.org/10.1016/B978-0-12-391857-4.00009-4.
62. Ritchie, M.E., Phipson, B., Wu, D., Hu, Y., Law, C.W., Shi, W., and Smyth, G.K. (2015). limma powers differential expression analyses for RNA-sequencing and microarray studies. Nucleic Acids Res. *43*, e47. https://doi.org/10.1093/nar/gkv007.
63. Silver, J.D., Ritchie, M.E., and Smyth, G.K. (2009). Microarray background correction: maximum likelihood estimation for the normal-exponential convolution. Biostatistics *10*, 352–363. https://doi.org/10.1093/biostatistics/kxn042.
64. Smyth, G.K., and Speed, T. (2003). Normalization of cDNA microarray data. Methods *31*, 265–273. https://doi.org/10.1016/s1046-2023(03)00155-5.
65. Struve, N., Binder, Z.A., Stead, L.F., Brend, T., Bagley, S.J., Faulkner, C., Ott, L., Müller-Goebel, J., Weik, A.S., Hoffer, K., et al. (2020). EGFRvIII upregulates DNA mismatch repair resulting in increased temozolomide sensitivity of MGMT promoter methylated glioblastoma. Oncogene *39*, 3041–3055. https://doi.org/10.1038/s41388-020-1208-5.
66. Budczies, J., Klauschen, F., Sinn, B.V., Győrffy, B., Schmitt, W.D., Darb-Esfahani, S., and Denkert, C. (2012). Cutoff Finder: a comprehensive and straightforward Web application enabling rapid biomarker cutoff optimization. PLoS One *7*, e51862. https://doi.org/10.1371/journal.pone.0051862.
67. Bankhead, P., Loughrey, M.B., Fernández, J.A., Dombrowski, Y., McArt, D.G., Dunne, P.D., McQuaid, S., Gray, R.T., Murray, L.J., Coleman, H.G., et al. (2017). QuPath: Open source software for digital pathology image analysis. Sci. Rep. *7*, 16878. https://doi.org/10.1038/s41598-017-17204-5.

STAR★METHODS

KEY RESOURCES TABLE

REAGENT or RESOURCE	SOURCE	IDENTIFIER
Antibodies		
Rabbit anti-Ki67 (for IHC)	Abcam	Cat # ab15580; RRID:AB_443209
Rabbit anti-Cleaved Caspase 3 (CC3) (175) (for IHC)	Cell Signaling Technologies	Cat # 9661; RRID:AB_2341188
Rabbit anti-ARHGAP12 (for IHC)	Novus Biologicals	Cat # NBP1-91678; RRID:AB_11011344
Rabbit anti-ARHGAP29 (for IHC and Western)	ATLAS antibodies	Cat # HPA026534; RRID:AB_1844998
Monoclonal mouse anti-E-cadherin (for IHC)	Abcam	Cat # ab1416; RRID:AB_300946
Monoclonal mouse anti-N-cadherin (for IHC)	Santa Cruz	Cat # Sc-59987; RRID:AB_781744
Rabbit anti-Vimentin (for IHC)	Abcam	Cat # ab16700; RRID:AB_443435
Actin Cytoskeleton/Focal adhesion kit	Merck	Cat # FAK100
Rabbit anti-Fyn	CST	Cat # 4023; RRID:AB_10698604
Rabbit anti-Lyn	CST	Cat # 2732; RRID:AB_10698604
Monoclonal mouse anti-Src	ThermoFisher Scientific	Cat # AHO1152; RRID:AB_1500518
Rabbit anti-E-cadherin	CST	Cat # 3195; RRID:AB_2291471
Rabbit anti-N-cadherin	CST	Cat # 13116; RRID:AB_2687616
Rabbit anti-Vimentin	CST	Cat # 5741; RRID:AB_10695459
Monoclonal mouse anti-GFAP	CST	Cat # 3670; RRID:AB_561049
Rabbit anti-Beta-catenin	CST	Cat # 9561; RRID:AB_331729
Rabbit anti -Non pBeta-catenin	CST	Cat # 19807; RRID:AB_2650576
Rabbit anti-Actin	ThermoFisher Scientific	Cat # PA5-78715; RRID:AB_2745831
Rabbit anti-RhoA	Abcam	Cat # ab86297; RRID:AB_10675086
Rabbit anti-Rac1	Abcam	Cat # ab155938
Biological samples		
Human GBM; 'TMA19'	Prof Michel Mittelbronn	N/A
Chemicals, peptides, and recombinant proteins		
6 BIO-indirubin	Selleckchem	Cat # S7198; CAS No. 667463-62-9
Dasatinib	Selleckchem	Cat # S1021; CAS No. 302962-49-8
Deposited data		
Raw and analysed microarray data	This paper	https://www.ebi.ac.uk/biostudies/arrayexpress/studies/E-MTAB-12775 deposited at BioStudies, EMBL-EBI
Experimental models: Cell lines		
Human: U87 MG	ATCC	HTB-14
Human: U87 MG non target control	This study	N/A
Human: U87 MG ARHGAP12 kd (stable)	This study	N/A
Human: U87 MG ARHGAP29 kd (stable)	This study	N/A
Human: U251 MG	ECACC	09063001
Human: U251 MG Non target control	This study	N/A
Human: U251 MG ARHGAP12 kd (stable)	This study	N/A
Human: U251 MG ARHGAP29 kd (stable)	This study	N/A
Experimental models: Organisms/strains		
Mouse: Balb/c nude	Charles River	RRID:SCR_003792

(*Continued on next page*)

Continued

REAGENT or RESOURCE	SOURCE	IDENTIFIER
Oligonucleotides		
shRNA ARHGAP12; ATAGTAATAGCAACGCCCT	Dharmacon	Cat # V3LHS_342870
shRNA ARHGAP12; TAGGTTGACAGTCTGACCT	Dharmacon	Cat # V3LHS_342873
shRNA ARHGAP 12; ATCACAATCTTTCTGTCCT	Dharmacon	Cat # V3LHS_342874
shRNA ARHGAP29; AAATGTTCCAAGGGAATTG	Dharmacon	Cat # V2LHS_68659
shRNA ARHGAP29; TTGGAACAAACAGTAGTAG	Dharmacon	Cat # V2LHS_68660
shRNA ARHGAP29; TATATCTGCACTGTTAGAG	Dharmacon	Cat # V2LHS_68661
Recombinant DNA		
psPAX2	Dr Chiara Galloni, University of Leeds	N/A
pMD.2GH	Dr Chiara Galloni, University of Leeds	N/A
Software and algorithms		
ImageJ	Rueden et al.,[56]	https://imagej.nih.gov/ij/
MTrackJ	Meyerlin et al.,[57]	N/A
Migration tool	Ibidi	Chemotaxis and Migration Tool | Free Software | ibidi
Cloudbuster	Rohwedder et al.,[25]	https://github.com/ARRohwedder/Cloudbuster
QuPath	Bankhead et al.,[58]	https://qupath.github.io/
Betastasis	Betastasis	https://www.betastasis.com
LIMMA	LIMMA	https://www.bioconductor.org
BioNavigator	PamGene	https//pamgene.com
Incucyte Woundmaker Tool	Incucyte/Sartorius	https://www.sartorius.com/download/950332/incucyte-scratch-wound-cell-migration-invasion-manual-en-840-1–data.pdf
ImageScope	Leica Biosystems	Aperio ImageScope | Pathology Slide Viewing Software
InkScape	Inkscape	https://inkscape.org

EXPERIMENTAL MODEL AND STUDY PARTICIPANT DETAILS

Cell lines

The established human glioma cell lines U87 (obtained from American Type Tissue Collection) and U251 (obtained from European Collection of Authenticated Cell Culture) derived from GBM used in this study were grown in DMEM supplemented with 10% foetal calf serum (FCS, Sigma, Dorset, UK; Cat # 7524) and penicillin/streptomycin in a CO_2 incubator. Cell lines had been authenticated inhouse by short tandem repeat (STR) profiling and were mycoplasma free.

The patient-derived GBM cell line E17 (classical GBM) was obtained from the CRUK Brain Tumour Centre of Excellence through the Glioma Cellular Genetics Resource funded by Cancer Research UK via MTA agreement (Steven Pollard, University of Edinburgh). The cells had been extensively profiled at the CRUK Brain Tumour Centre[56] and mycoplasma tested upon receipt at the University of Huddersfield. The E17 cell line was cultured as advised by the CRUK Brain Centre in laminin coated T-25 flasks (Corning, UK) in complete media constituted of DMEM/HAMS-F12 (Gibco, Paisley, UK, cat # 12634028), containing 1.45% glucose (Sigma Life Science, Poole, UK; cat # G8644), 1% MEM NEAA (Minimum Essential Medium Non-Essential Amino Acids, Gibco, Paisley , UK cat # 11140-03) 100x, 1% penicillin streptomycin, 0.16% BSA (Bovine Serum Albumin, Gibco, Paisley, UK; cat # 15260-03), 0.2% mercaptoethanol (Gibco, Paisley, UK; cat # 31350-01), 1% B27 supplement and 0.5% N2 supplement (all Fisher Scientific, Loughborough, UK; cat # 17504-04, # 17504-04). Before use, this was supplemented with mouse EGF and human FGF (both Peprotech, ThermoFisher Scientific, Altrincham, UK; cat # 315-09, # 100-18b), to a final concentration of 10 ng/ml and laminin (Bio-Techne, Abingdon, UK; cat # 3446-005) to a final concentration of 2 μg/ml.

The primary, patient-derived GBM cell line CX18 Core 1 (Female; Late 50's; left frontal GBM tumour) was obtained from Dr Ola Rominiyi and Professor Spencer Collis (University of Sheffield, UK). The cells were cultured as previously described by these authors[57]; briefly, GSC cultures were maintained in stem cell enriching conditions using 'stem media'. This consisted of Adv DMEM F12 medium (Gibco, Paisley, UK; cat # 12634028) supplemented with 1% B27 (Gibco, Paisley, UK; cat # 17504-044), 0.5% N2 (Gibco, Paisley, UK; cat # 17502-048), 4μg/ml heparin (Sigma, Poole, Dorset, UK; cat # H3393-10KU), 20ng/ml epidermal growth factor (EGF) (Novus Biologicals, Cambridge, UK; cat # NBP2-34952), 20ng/ml fibroblast growth factor (FGF) (Peprotech, ThermoFisher Scientific, Altrincham, UK; cat # 100-18b), 1% L-glutamine (Gibco, Paisley, UK; cat # 25030081), 1% penicillin-streptomycin (Sigma, Poole, Dorset, UK; cat # P4333) and 0.1% amphotericin B (Gibco, Paisley, UK; cat # 15290026). Monolayer glioma stell cell (GSC) cultures were seeded onto Matrigel™-coated plastic tissue culture flasks or plasticware. Cells were passaged when 70-80% confluency from microscopic appearance was reached. Cell lines were propagated as adherent monolayers in flat sided 75cm^2 tissue culture flasks containing 10ml complete stem media (GSC) in a humidified incubator at: 37°C, 5% CO_2 and 21% O_2. Once primary, patient-derived cell lines had been successfully established, media was replaced every 2-3 days and cells were routinely passaged roughly every 5-10 days, dependent on the cell line (typically splitting at a 1:5 ratio).

The primary, patient-derived GSCs were used at low passage following recent generation from freshly resected brain tumor tissue therefore cell authentication using STR profiling has not been performed at this stage. Baseline whole exome sequencing characterisation for the cell line was generated which will be made publicly available in due course (manuscript in preparation). In addition, this cell line is planned to undergo baseline STR profiling later this year following modest dedicated funding to develop Sheffield Living Biobank as a research resource being recently secured.

The cell line was routinely tested for mycoplasma infection (typically each month whilst being cultured) and was not passaged beyond 15-20 times after thawing in order to avoid phenotypic drift.

In vivo experiments

12 week-old female nude Balb/c mice (bred in-house from an origin stock supplied by Charles River) were maintained in groups of five littermates in individually ventilated cages. The groups were assigned randomly. Cages contained sawdust, paper bedding and environmental enrichment. Mice were housed at 20 ± 2°C under a 12-hour light/12-hour dark photoperiod. They received standard rodent pelleted chow *ad libitum* (Special Diets Services, Witham, UK).

For orthotopic intracranial injections, animals were stereotactically injected (2.5 mm from the midline, 2.5 mm anterior from bregma, 3 mm deep) with 2 μl 1x10^5 cells each consisting per animal group of shRNA ARHGAP12, shRNA ARHGAP29 and shRNA non-target control U87 cells.

Surgery was performed under inhaled isoflurane using aseptic technique. Post-operatively, mice were monitored daily for signs of sickness, pain, or weight loss. Mice were sacrificed once symptoms of tumour formation were evident. Animals were sacrificed under terminal anaesthesia with transcardial perfusion of saline, followed by 4% paraformaldehyde fixative.

Animal brains were harvested, post-fixed *ex vivo* and cryopreserved in preparation for immunohistochemistry.

The work was licensed by the UK Home Office (P67C4EBE4) and complied with the guiding principles for the care and use of laboratory animals. Ethical approval was granted by University of Leeds Animal Welfare and Ethics Review Body and the UK Home Office (Animals [Scientific Procedures] Act 1986) and conducted in accordance with the University of Leeds Policy on the Use of Animals in Scientific Research and the ARRIVE Guidelines.

GBM tissue microarray (TMA)

We used an in-house 'TMA19' consisting of 60 number of cases of GBM and the following clinical data, date of birth, day of surgery, age, survival, sex, WHO grade, type of tumour (primary/secondary), recurrence, sample site, tumour infiltration, Karnofsky-score, tumour localisation, presence of oedema, full resection, radiation, chemotherapy, steroid treatment, MIB-index, p53, pHH3, IDH1, ATRX, MGMT status, 1p (LOH) and Chr 19 presence. The TMA section was gifted by Professor Michel Mittelbronn and had been part of a wider study as described by Michelbronn et al.[59]

METHOD DETAILS

Main reagents

The GSK-3 inhibitor bromoindirubin-3-oxime (BIO) (Selleckchem, Ely, UK; cat # S7198) in DMSO was prepared as predetermined working dilutions (5 μM) in the appropriate culture medium. The multi-targeted Src kinase inhibitor Dasatinib (Selleckchem, Ely, UK; cat # S1021) in DMSO was also prepared as predetermined working dilution (10 μM) in the appropriate culture medium.

The following antibodies were used for immunocytochemistry studies and immunohistochemistry, Ki67 (1:5000, Abcam, Cambridge, UK; Cat # ab15580), Cleaved Caspase 3 (CC3) (1:100, Cell Signaling Technologies, New England, UK; Cat # D175), ARHGAP12 (1:200, Novus Biologicals, Cambridge, UK; Cat # NBP1-91678), ARHGAP29 (1:100, ATLAS Antibodies, Cambridge, UK; Cat # HPA026534), E-cadherin (1:100, Abcam, Cambridge, UK; Cat # ab1416), N-cadherin (1:100, Santa Cruz Biotechnology, Heidelberg, Germany; Cat # Sc-59987), Vimentin (1:200, Abcam, Cambridge, UK; Cat # ab16700), Actin Cytoskeleton/Focal adhesion kit (1:500, Merck, Feltham, UK; Cat # FAK100).

Live cell imaging

Cells were seeded at subconfluence in Ibidi imaging dishes (Ibidi, Graefeling, Germany; Cat # 80146) in CO_2 independent medium (ThermoFisher Scientific, Altrincham, UK; Cat # 18045088) supplemented with 10% FCS and essential minerals with or without the inhibitor or after transient/stable kd. They were imaged over 24 -72-hour periods at 3 min intervals on a BioStation IM imaging system (Nikon, Surbiton, UK). Movies were generated from AVI files and used for data analyses with ImageJ[60] and the MtrackJ plugin.[61] At least 50 cells/condition were used for analysis of velocity and displacement. Rose plots were generated with the Ibidi Migration Tool (Chemotaxis and Migration Tool | Free Software | ibidi). All experiments were repeated 3 times. For imaging with the IncuCyte system (Essen BioScience, Newark, UK) cells were maintained in medium complemented with 10% FCS and with the GSK-3 inhibitor BIO (5 μM) (Selleckchem, Ely, UK; # S7198) in flat bottom 96 well plates (Nunc, Altrincham, UK; Cat # Z688665). Data was generated using IncuCyte software and ImageJ.

For 3D migration, U87 and U251 spheroids were generated in 96 well low adherence plates (Sigma, Poole, Dorset, UK; Cat # 7007), as previously reported.[19] Briefly, $1x10^3$ cells/well were allowed to incubate in the low adherence plates for 72 hours. After spheroid formation, the original growth medium was replaced with a collagen matrix consisting of rat tail collagen type I (Sigma, Poole, Dorset, UK; Cat # CLS354236), and 5x growth medium which was then semi-polymerised by the addition of 1 M NaOH. Growth medium was added (containing inhibitor or no inhibitor depending on the experimental set-up) at a collagen:medium 1:1 ratio. After implantation into the collagen matrix, cell protrusions/single cells were allowed to migrate into the collagen for 72 hours. Imaging of the spheroids was achieved at 24h timepoints with the EVOS imaging system (ThermoFisher, Altrincham, UK).

Immunofluorescence assays

For immunofluorescence assays cells were seeded at subconfluence; for inhibitor assays they were treated for between 8 and 72 hours with the appropriate inhibitor. Cells were fixed with 4% paraformaldehyde, followed by permeabilization with 0.05% Triton-X-100 (Sigma, Poole, Dorset, UK; Cat # 9002-93-1). After 3 washes in PBS they were blocked with 0.05% Marvel skimmed milk powder solution for 5 min. The block was removed, and primary antibody solution was added. All antibodies were prepared in the blocking solution and spun for 5 min at > 10,000g in a microcentrifuge prior to use. All incubations were carried out in a humidified incubation chamber; PBS was used for 3 washes (5 minutes/wash) between incubations. After incubation with the primary antibodies for 1 h and 3 washes (5 minutes/wash) with PBS the cells were incubated with the secondary antibodies in blocking solution and 4',6-Diamidino 2-Phenylindole (DAPI) (Molecular Probes, ThermoFisher, Altrincham, UK; Cat # D1306) was used as a marker of DNA. All slides were mounted in Fluoromount G (Southern Biotech, Birmingham AL, USA; Cat # 0100-01) after a final set of 3 washes with PBS.

For immunofluorescence assays of spheroids the method described by Cheng et al.[19] was followed. Spheroids maintained in the original collagen insert were washed 3 times with PBS. They were fixed with 4% paraformaldehyde for 30 min at room temperature followed by permeabilisation with 0.05% Triton-X100 (Sigma, Poole, Dorset; Cat # 9002-93-1) for 15 min. After another 3 washes with PBS, they were blocked with 0.05% Marvel skimmed milk powder. The antibody solutions were added in the same blocking buffer after centrifugation for 5 min at > 10,000g. They were incubated for 2 h at room temperature. Another 3 washes with PBS were followed by incubation with the secondary antibodies for 1 h. DAPI was added as described above. After incubation with the secondary antibody, the collagen plugs were washed 3 times with PBS and then carefully lifted out of the 96 well plates and placed onto glass slides. Drops of Fluoromount G (Southern Biotech, Birmingham, AL 35209, USA; Cat # 0100-01) were added to the collagen plugs and cover slips were added.

Bioinformatics

A Betastasis (http://www.betastasis.com) search was carried out utilising the Cancer cell line encyclopaedia and the gene expression bar plot function (Sample group: Central Nervous system) (Affymetrix HG U133 Plus 2.0). According to the website, raw Affymetrix CEL files were converted to a single value for each probeset using RMA and quantile normalization. The probeset used was ENTREZG v15 from the BrainArray project.

Microarray analysis

Samples from U251 cells treated for 24 hours with BIO (5 μM), prepared and extracted according to Agilent instructions, were run on Agilent SurePrint G3 Human Gene Expression 8x60K v2 arrays. 6 arrays were used on each slide (using 2 dyes). The slides were processed and analysed in house (Leeds MRC Medical Bioinformatics Centre). Microarray data were processed in R using the LIMMA[62] package as follows: First, per-array correction was performed using a normal and exponential convolution method (''normexp'')[63,64] followed by LOESS normalisation of the multiple subarrays on each chip. Multiple arrays were normalised using quantile normalisation across the average intensity values (''Aquantile'').[58]

Differential gene analysis was also performed using LIMMA (samples were normalised against cell line, treatment, and time point). Results were computed using a 2-colour linear model followed by empirical Bayes moderation of the standard errors. Multiple testing correction was performed using Benjamini & Hochberg False Discovery Rate (FDR) adjustment. An FDR threshold of 0.001 was applied to select only highly significant genes.

ARHGAP12 siRNA

U251 or U87 cells were transfected with either 50nM or 100nM siRNA. The transfection mix consisted of siRNA incubated with RNAiMAX Lipofectamine (1/200) (ThermoFisher Scientific, Altrincham, UK; Cat # 13778030) and OPTI-MEM™ (Thermofisher Scientific, Altrincham, UK; Cat # 51985034) for 10 min at room temperature. The siRNA used were ONTARGETplus SMARTpool ARHGAP12 (94134) (ThermoFisher Scientific Dharmacon, Lafayette, Colorado, USA). After complex formation, the mix was added to corresponding wells and then cells added and gently pipette mixed. For live cell imaging, Ibidi dishes (Ibidi, Geafeling, Germany; Cat # 80146) were used; 100 μl of siRNA mix and 500 μl cell suspension (5000 cells/condition) were added to the individual dish segments. For RNA isolation 6 well dishes were used (ThermoFisher Scientific, Altrincham, UK; Cat # 150239); to each well 500 μl siRNA mix and 2ml cell suspension (300,000 cells/well) were added.

For 3D invasion assays, low adherence 96 well plates (Sigma, Poole, Dorset, UK; Cat # 7007) were used to generate spheroids. During aggregate/spheroid formation 20 μl siRNA mix and 80 μl cell suspension (1000 cells/well) were added. The spheroids were allowed to form over 72 h.

ARHGAP29 siRNA

Reverse transfection was performed using RNAiMAX lipofectamine (Invitrogen, Life Technologies, Altrincham, UK; Cat # 13778-075), OPTI-MEM® I Reduced Serum Medium (Gibco™, Invitrogen corporation, Altrincham, UK; Cat # 31985). 50mM or 100mM of siRNA against ARHGAP29 using 4 individual siRNA sequences were included (HorizonDiscovery, Lafayette, Colorado, USA; ON-Targetplus siRNA; Cat # 9411). U251 cells well seeded at $2x10^5$ cells per well in 6-well plates. For each siRNA concentration, one plate was harvested for RNA and one plate for protein lysates 72h post transfection.

Real Time PCR

RNA was isolated and purified using the Qiagen RNA easy mini kit protocol (Qiagen, Manchester, UK; Cat # 74104). For reverse transcription, the Applied Biosystems highcapacity reverse transcription cDNA kit (Applied Biosystems, Warrington, UK; Cat # 4368814) was used according to manufacturers' instructions. 50ng corresponding cDNA per well was added to each well of an Applied Biosystems™ MicroAmp™ Optical 96-Well Reaction Plate (Applied Biosystems, Warrington, UK; Cat # N8010560). Samples were measured in triplicate with 3 technical repeats per condition. 10 μl of Taqman Mastermix and 1 μl of ARHGAP12 or ARJHGAP29 target primer probe sets or 18S endogenous control primer probe set probe (1 μl) were used. Samples were run on the Applied Biosystems 7500 real time PCR analyser and Relative quantification (RQ) (=2-ΔΔCtRQ) values measured using the analyser software (Applied Biosystems, Warrington, UK) were normalised to control samples.

Small hairpin RNA

Gene silencing shRNA of ARHGAP12 and ARHGAP29 was achieved by insertion of shRNA via GIPZ lentiviral transduction. Three separate constructs targeting ARHGAP12 (V3LHS_342870, V3LHS_342873, V3LHS_342874) and ARHGAP29 (V2LHS_68659, V2LHS_68660, V2LHS_68661) were obtained from Dharmacon. Reaction mixes containing the ARHGAP plasmids, pPAX2 and pMD.2GH vector, OPTI-MEM (Gibco, Altrincham, UK; Cat # 51985-026) and Lipofectamine 2000 (Thermofisher, Altrincham, UK; Cat # 11668019) were set up and used to transfect Lenti-X cells seeded at $4x10^6$/10 cm^2 petri-dishes coated with fibronectin (Sigma, Poole, Dorset, UK; Cat # F0895-5MG) 24 h prior to transfection. The cells were incubated, and medium changed after 24 h. Over the next 2 days supernatants were harvested and filtered with a 0.45 μM filter (Millipore Sigma, Poole, Dorset, UK; Cat # SLHA02510) and stored at 4°C until further use. U251 or U87 were plated in 6 well dishes in duplicate at $1x10^5$/2ml to reach approximately 70% confluence by the following day. For transduction, the supernatants were added to the 6 well dishes (2ml/well) and the cells were allowed to incubate for 24h. Cells were viewed by immunofluorescence microscopy to assess transduction efficiency as detected by green fluorescence. Cells were then reseeded in tissue culture flasks in the presence of puromycin (10 μg/ml) (Sigma, Poole, Dorset, UK; Cat # P8833) as selection medium. As a control we also concluded a non-target construct. Kd efficiency was confirmed by immunofluorescence and western blotting. All cells were then used for initial live cell imaging and invasion assays to assess the effect on cell migration. The constructs eliciting the greatest effect on cell migration were used in all further studies. The same shRNA construct was used to silence ARHGAP29 in both U87 and U251 (V2LHS-68659), abbreviated to '59' in this study, whilst two different shRNA constructs were required to silence ARHGAP12 in U87 (V3LHS-432870), abbreviated to '70' and U251 (V3LHS-342874), abbreviated to 74.

Phenotypic analysis for ARHGAP shRNA kd

For phenotypic analysis, ARHGAP kd cells and non-target control cells (both U87 and U251) were plated at subconfluence, incubated for 24 hours at 37°C and then fixed with 4% PFA. The cells were stained with Phalloidin 594 and DAPI as previously described. For analysis of phenotype, i.e. localisation of the actin cytoskeleton, at least 200 cells/condition were scored. The experiment was repeated three times.

Pulldown assay

For the pulldown analysis, a pulldown kit by ThermoScientifc (Active Rho Pull-Down and Detection kit; ThermoFisher, UK; Cat # 16116) was used following manufacturer's instructions. To prepare lysates for the assay, U251 cells were plated at subconfluence and incubated for 24 hours at 37°C with Bio-indirubin (5 μM) or DMSO only (0.05%). Lysates were then prepared as per

manufacturer's instruction. The provided negative and positive controls were also used in this assay. A Biorad minigel system was used to run lysates on a 4-12% gradient gel; proteins were transferred with a Biorad Trans-Blot Turbo transfer system and the western blotting was carried out following manufacturer's instructions.

Rac1/RhoA G-LISA

Rac1/RhoA activation was measured using the Rac1/RhoA G-LISA activation assay (Cytoskeleton inc, Denver, CO 80223, USA; Cat # BK124) as per the manufacturer's instructions. U87 and U251 at subconfluent level were treated with BIO and allowed to grow for 24h. The cells were lysed and RhoA1 or Rac1 activity was measured colorimetrically at 490 nm. Cell lysates were used in triplicates.

Functional kinome profiling

Functional kinase activity profiling has been described previously.[65] Here we used a PamStation®12 (located at the UCCH Kinomics Core Facility, UKE, Hamburg, Germany) according to the manufacturer's instructions (PamGene International, 's-Hertogenbosch, The Netherlands). In brief, for profiling serine-/threonine kinases and tyrosine kinases, STKPamChip® and PTK-PamChip® arrays were used, respectively. Each array contains 140 individual labelled-site(s) that are peptide sequences derived from substrates for serine/threonine kinases or tyrosine kinases. Whole cell lysates were prepared using M-PER Mammalian Extraction Buffer containing Halt Phosphatase Inhibitor and EDTA-free Halt Protease Inhibitor Cocktail (Pierce, Waltham, Massachusetts, USA; Cat # 78440). For STK arrays 1 μg, for PTK arrays 5 μg of protein and 400 μM ATP were loaded. Sequence-specific peptide tyrosine phosphorylation was detected by the fluorescein–labelled antibody PY20 (Exalpha, Maynard, MA, USA; Cat # X1017S) and a CCD camera using the Evolve software (PamGene International, 's-Hertogenbosch, The Netherlands). Serine-threonine phosphorylation was detected in two steps, first with anti-phospho-Ser/Thr antibodies during the reaction followed by detection with secondary antibody (polyclonal swine anti-rabbit Immunoglobulin/FITC, PamGene International). After quality control the final signal intensities were log_2-transformed and were used for further data analysis using the BioNavigator software version 5.1 (PamGene International, 's-Hertogenbosch, The Netherlands).

SDS-PAGE and western blotting

Adherent sub-confluent to confluent cell cultures were harvested on ice as follows: Cells were washed three times with ice cold Dulbecco's phosphate buffered saline (PBS, 137 mM NaCL, 2.7 mM KCL und 12 mM phosphate, pH 7.4) and collected in ice cold PBS with a cell scraper, transferred to a 2 ml centrifugation tube and pelleted for 5 min at 650 x g at 4°C. Cell pellets were either directly processed or stored at −80°C for later use.

Pelleted cells were resuspended in 200 μl Tris-Triton lysis buffer (20 mM Tris-HCl, pH 8, with 137 mM NaCl, 1% TritonX100, 2 mM EDTA, 10 % Glycerol), supplemented with Pierce Protease Inhibitor cocktail (ThermoFisher Scientific, Altrincham, UK; Cat # A32963) by vortexing. The cell suspension was rotated end-over-end for 30 min at 4°C and syringed by 10 – 20 strokes through a 0.8 mm hypodermic needle. Cell lysates were centrifugated at > 10,000 x g for 10 min at 4°C and the resulting cleared lysates were transferred to a pre-cooled 1.5 ml centrifugation tube and stored at −80°C if not immediately used.

Protein concentrations of cleared cell lysates were determined spectrophotometrically following standard Bradford protein assay protocol and equal amounts of protein were diluted with 2 x SDS sample buffer (2 x Laemmli buffer, 100 mM Tris-HCl, pH 6.8, 20 % Glycerol, 4 % SDS, 0.4% Bromophenol blue, supplemented with 2% SDS and 10% β-mercaptoethanol or 1 mM DTT prior to use) and boiled for 5 min at 95°C. Proteins were separated on 7.5 % or 4 - 20% PAGE (MiniProtean TGX™ pre-cast gels, BioRad, Watford, UK; Cat # 4561023; Cat # 4561094) in Tris/Glycine buffer (25 mM Tris, 192 mM glycine) with 0.1 % SDS and transferred to a PVDF membrane (BioRad, Watford, UK; Cat # 1620177) by wet electroblotting (90 min at 250 mA) in Tris/Glycine buffer with 20% methanol.

For immunodetection PVDF membranes were briefly washed with PBS and blocked in PBS-Tween 0.05% with 5% non-fat dry milk (Morrisons, Bradford UK) (anti-ARHGAP 12 and anti-ARHGAP 29), or 3% BSA (all other antibodies) for 30 min at room temperature with light agitation, followed by primary antibody incubation at 4°C overnight with primary antibodies diluted in 2% blocking solution. Used primary antibodies were obtained from Atlas Antibodies (ARHGAP12, Cat # HPA000412; ARHGAP29, Cat # HPA026534), Cell Signaling Technologies (Fyn, Cat # 4023; Lyn, Cat # 2732; E-cadherin, Cat # 3195; N-cadherin, Cat # 13116; Vimentin, Cat # 5741; GFAP, Cat # 3670, beta-catenin, Cat # 9561, Non-Phospho (P) - beta-catenin, Cat # 19807), ThermoFisher (pan-Actin, Cat # PA5-78715; cSrc, Cat # AHO1152), Abcam (RhoA, Cat # ab86297; Rac1, Cat # ab155938) and incubated at recommended manufacturer's dilutions. After primary antibody incubation membranes were washed with PBS-Tween 0.05%, and incubated with respective secondary HRP-conjugated antibodies (ThermoFisher Scientific, Altrincham, UK; Cat # 1620177; Cat # 31460) in 2% blocking solution for 90 min at room temperature. Membranes were carefully washed with PBS-Tween 0.05% and PBS. Chemoluminescence was detected with ECL Clarity (BioRad, Watford, UK; Cat # 1705060) on X-ray film and additionally imaged with a G-Box imager (Syngene, Cambridge; UK).

Src kinase siRNA studies

SiRNA transfections were carried out according to manufacturer's recommendation. Briefly, U251 cells were transfected with 3μl Lipofectamine (ThermoFisher Scientific, Watford; Cat # L3000001), 4μl 2nM siRNA in 1.5 ml DMEM, containing 1% FCS (Sigmal, Poole, Dorset, UK; Cat # F7524) each. For determination of average number of large protrusions detected in control (scrambled) versus siRNA treated U251 cells (siFyn, Santa Cruz, Wembley, UK; Cat # SC-29321; siLyn, Cat # SC-29393; siSrc,

Origene,Wembley, UK; Cat # SR321884) cells were grown in 1% FCS containing DMEM overnight and fixed with 1% PFA at room temperature. Cells were stained with 3-hexanoyl-NBD cholesterol (Cayman Chemicals, Cambridge, UK; Cat # 13221) for 10 min on ice, washed twice with cold PBS and embedded in Mowiol 4-88 (Sigma Aldrich, Poole, UK; Cat # 81381) on a glass slide. Images were recorded using Leica LSM 700 with 60x magnification oil immersion. The ImageJ plugin has been described before.[4]

Quantification of relative wound closure speed

Data were derived from the Incucyte (Sartorius, Epsom, UK) wound healing assay for siRNA treated U251 cells, grown overnight in DMEM with 1% FCS. Cells were seeded in flat-bottom 96-well plates to reach confluence before measurement and the assay was set up using the Incucyte Woundmaker Tool (Sartorius, Epsom, UK; Cat # BA-04858). Quantification of wound closure was based on the generated bright field images.

Src kinase inhibitor studies

U251 cells were plated at subconfluence and incubated for 24 hours at 37°C with Dasatinib (10 μM) (Selleckchem, Ely, UK; Cat # S1021) or DMSO only (0.05%). After incubation cells were fixed with 4% PFA as previously stated and stained with DAPI and Alexa Fluor Phalloidin-594 (Molecular Probes, ThermoFisher, Altrincham, UK; Cat # D1306 and cat # A12381). The cells were imaged by confocal microscopy and images averaging at least in total 200 cells/condition were analysed for the different phenotypes, ie, cells with cortical actin/stress fibres/'other'. The experiment was repeated three times.

Immunohistochemistry

Further details for the immunohistochemistry of the spheroids, mouse brain tissue and tissue microarrays, along with the analysis is outlined in the supplemental information.

Survival analysis of patient data

Dichotomisation of data was achieved by generating received operator characteristic (ROC) curves to obtain relevant cutoffs[66] for low and high protein expressors. Disease-free survival (DFS; from initial diagnosis to the diagnosis of local or distant recurrence) and overall survival (OS; from initial diagnosis to death) associations were analysed by Kaplan–Meier plots (log rank test). Hazard ratios (HR) were determined by Cox regression. Patient follow up data was available for at least 2 years and was last updated in MONTH YEAR and survival periods calculated. Patients were censored from the study at the last date they were known to be alive. Variables were entered in univariate and multivariate analysis (Cox proportional hazards regression model) in IBM SPSS Statistics (v25).

Immunohistochemistry spheroids

The protocol for generating sections from glioma spheroids was previously described[19]; spheroids were immunostained with ARHGAP12 and ARHGAP29 antibodies. Both antibodies were optimised for use on glioma spheroid sections. Briefly, after completion of the experiment, spheroids were washed three times in PBS whilst still maintained within their collagen plugs in the low-adherence well plates. They were then fixed in 4% PFA for 24 h at 21°C covered with foil prior to tissue processing and paraffin wax embedding. After wax embedding, specimens were sectioned into 5 μm thin slices through the diameter of the spheroid core. Sections were used for staining with the antibodies.

In vivo mouse brain tissue

Brain cryosections were stained for Vimentin (for tumor identification/marker of aggressiveness), Ki67 (proliferation marker), Cleaved Caspase 3 (CC3) (apoptosis marker), E-cadherin and N-cadherin. The IHC protocol as previously described was followed.[54] Briefly, antigen retrieval was completed using Access Revelation (MenaPath) retrieval buffer (A. Menarini Diagnostics, Wokingham, UK; Cat # MP-607). Optimisation of antibodies was performed using reference tissue before staining experimental tissue. All antibodies were diluted in antibody diluent reagent solution (Invitrogen, Altrincham, UK; Cat # 00–3218) and incubated at room temperature for 1 h. All staining using rabbit antibodies (Ki67, 1:5000; Cleaved caspase 3 (CC3), 1:100; ARHGAP12, 1:200; ARHGAP29, 1:100; Vimentin, 1:200) was performed using ImmPRESS HRP Anti-Rabbit IgG kit (VECTOR laboratories, UK; Cat # MP-7401) as per the manufacturer's instructions. The staining using mouse antibodies (E-cadherin, 1:100; N-cadherin, 1:100) was performed using M.O.M ImmPRESS peroxidase polymer Kit (VECTOR laboratories, Orton Southgate, UK; Cat # MP-2400). The chromogen substrate used was 3, 3'diaminobenzidine (ImmPACT DAB Peroxidase Substrate Kit by VECTOR laboratories, Orton Southgate, UK; Cat # SK-4100). Cell nuclei were counterstained using Mayer's haematoxylin followed by differentiation in lithium carbonate.

Histological analysis

The stained slides were scanned with an Aperio CS2 scanning system (Leica Biosystems). The images were analyzed both manually and automatically using QuPath (https://qupath.github.io).[67] All the positively stained cells were counted using QuPath (version 0.1.2). A region of interest (ROI) was manually defined in each histological whole slide image, ensuring any artifacts were excluded. The ROI was the GBM tumor mass defined by using the vimentin-stained slides for reference. Positive cell detection thresholds and other parameters for cell detection and classification were adjusted manually for each staining type and then applied uniformly across

all samples in the cancer cohort. All automation scripts were validated by a Neuropathologist (AI) to confirm accurate detection of the tumors.

Surface roundness/smoothness of vimentin-stained tumors

Vimentin-stained slices were processed first as the intensity and homogeneity of the staining aided the definition of the borders between tumor sites and normal brain tissue. Initially, the negative pen tool of ImageScope (Leica Biosystems) was used to manually trace the smoothest/roundest area, <0.1 μm^2 from the tumor's defined border. Tracing of the tumor surface, for each vimentin-stained tumor slice, was repeated at least in triplicate, each time with deletion of the previous tracing event, to generate adequate technical replicates for statistical testing. Subsequently, tumor surfaces were traced precisely so that roughness, indentations, protrusions, and potential hypoxic breakages were represented in the recorded trace, and surface area readouts were collected at least in triplicate again. Differences between the roughly smoothest and detailed uneven surface areas for each tumor site were expressed as a percentage of deviation from smoothness/roundness.

To measure the length of the ''smooth'' and the ''non-smooth'' tumor perimeter, 8-10x magnified screenshots of individual brain slices from ImageScope, were saved and imported into ImageJ.[56] For determination of the 'smooth' tumor perimeter, images were converted to greyscale (8-bit) and a Gaussian blur (3–5 px area according to the processed tumor) was applied to aid border detection though threshold adjustment of the black and white channels.

A hollow black object was generated, and its surface was calculated, by selecting the ''analyze particle'' option from the analysis menu, once the scale of the object was set to reflect its actual dimensions. Similarly, the same process was used for the automated calculation of the ''nonsmooth'' tumor perimeter, except that the blurring step was omitted or used at 2 px if needed. In addition to particle surface area, particle analysis revealed value and position of centroids which used to define tumor epicentres. Comparisons between the defined surface areas (smooth versus non-smooth) were again used to define deviations from roundness/smoothness, similar to the manual approach, thus generating an additional set of data for technical replicate tests.

ImageJ generated particles were saved as bmp files and further processed through Inkscape (https://inkscape.org) for the generation of high-quality tumor cartoons. Firstly, bmp images were automatically traced to generate appropriate vector graphics. The vectors were individually colored and shaded, and their centroids were used to align the overlay images.

Quantification of cell detachments from tumor mass

Cell detachments within tumors were assessed in 3 zones, namely core, periphery (including those with <0.1 mm distance from tumor border) and outside, using ImageJ. Detached cells and/or detached clusters from tumor mass were manually counted and their distances from the tumor center were measured and recorded. All selected distances were sent to the ROI manager for individual processing and for the generation of radial overlays. Radial overlays were saved as bmp images and further processed in Inkscape to generate vector graphics. A basic image of concentric circles with different radii (ranging from 0.25–3.00 mm) was generated in Inkscape and used to further align the outline vector graphic of the tumor and the radial overlay of the detachments from its centroid. To complete the display of these radial graphs, clockwise and counterclockwise angle directions were included. Numbers of cell detachments were normalised to tumor surface area.

Analysis of single migratory cells and cell protrusions

For analysis of single migratory cells and cell protrusions brain slices labeled with the Vimentin antibody were utilised. QuPath software was employed to identify Vimentin-positive tumor cells in the surrounding brain parenchyma or directly adjacent to tumor tissue. Highlighted cells or cell groupings were measured for length, perimeter, and size. Cell roundness was established using the QuPath analysis application; the resultant 'roundness' index allowed determination of a rounded cell morphology with 1 equal to a perfect circle.

TMA

Immunohistochemistry staining using mouse antibodies

For staining, the TMA slides were dewaxed in 4 sequential xylene baths for 5 min each followed by rehydration through sequential washes in descending concentrations of ethanol, before a final rinse in running tap water.

Rehydrated tissues underwent heat-induced antigen retrieval using a pressure cooker system, whilst bathed in a citrate buffer (pH6). After antigen retrieval, the slides were first subjected to endogenous hydrogen peroxidase blocking with Bloxall (Vector Laboratories, Orton Southgate, UK; Cat # SP-6000) for 10 min. After a wash with Tris-buffered solution Tween (TBST) for 5 min, protein blocking was performed with 1/10 casein (Vector Laboratories, Orton Southgate, UK; Cat # SP-5020) for 20 min. Immediately after blocking without washing the slide the primary antibodies were added at and incubated for 1h at room temperature. The slides were then washed twice with TBST for 5 min each, and then stained with ImmPRESS Exel staining Kit Peroxidase anti mouse (Vector Laboratories; Orton Southgate, UK; Cat # MP-7602) or anti-rabbit polymer (Menapath, A. Menarini Diagnostics, Wokingham, UK; cat # MP-XCP- P0100) following the manufacturer's instructions. Slides were washed 2x with TBS for 5 min each, followed by staining with 3, 3'diaminobenzidine (DAB) Chromogen substrate (ImmPACT) (Vector Laboratories, Orton Southgate, UK; Cat # ImmPACT

SK-4105). Cell nuclei were counterstained (blue) with Mayer's haematoxylin for 30 s. Slides were washed under a fast-flowing tap for 1 min before immersing in Scott 's Tap Water for 1 min and a final rinse in tap water for 1 min. The sections were dehydrated and mounted with a glass coverslip.

TMA analysis

For TMA analysis cores were scored manually for presence of protein, protein expression levels and protein location. Protein presence was quantified as the proportion of cells positively stained (brown color) compared to non-stained cells, categorised as: no stain = 0%, 1–25% = 1; 26–50% = 2; 51–75% = 3 and 76–100% = 4. Protein expression was semi-quantitatively measured according to staining intensity and categorised as follows: no staining = 0, weak = 1, medium = 2, and strong = 3. The staining levels from both scores were combined to give a maximum overall score of 7.

QUANTIFICATION AND STATISTICAL ANALYSIS

Statistical analysis

All results are reported as mean ± SD, unless otherwise stated. Statistical analysis was performed using GraphPad Prism (v.5.0; GraphPad Software, San Diego). Pairwise differences in mean were compared using a two-tailed Student's *t*-test. Mean differences in groups of 3 or more populations were compared using a one-way analysis of variance (ANOVA) and pairwise comparisons were made using a post-hoc Dunnett's test. For non-normal data, overall differences were analyzed by Kruskal-Wallis test, with pairwise comparisons of medians made using Mann-Whitney U tests. For categorical data, differences were compared using a Fisher's exact test. Survival data was displayed as Kaplan-Meier plots and differences in survival were compared using a log rank test. Hazard ratios were determined by Cox regression and variables were entered in univariate and multivariate analysis. Functional kinomics data were analyzed using BioNavigator software version 5.1 (PamGene International, 's-Hertogenbosch, The 759 Netherlands). Statistical significance was set at $p < 0.05$ for all tests. Statistical details of experiments can be found in the figure legends and associated result sections.